



Persistent luminescence of Eu/Dy-doped $\text{Sr}_2\text{MgSi}_2\text{O}_7$ glass-ceramics processed by aerodynamic levitation

L. Fernández-Rodríguez, Mathieu Allix, G. Gorni, A. Canizarès, S. Ory, G.C. Mather, A. Durán, D. Levy, M.J. Pascual

► To cite this version:

L. Fernández-Rodríguez, Mathieu Allix, G. Gorni, A. Canizarès, S. Ory, et al.. Persistent luminescence of Eu/Dy-doped $\text{Sr}_2\text{MgSi}_2\text{O}_7$ glass-ceramics processed by aerodynamic levitation. Journal of the European Ceramic Society, 2022, 42 (16), pp.7596-7608. 10.1016/j.jeurceramsoc.2022.08.062 . hal-03874464

HAL Id: hal-03874464

<https://hal.science/hal-03874464>

Submitted on 28 Nov 2022

HAL is a multi-disciplinary open access archive for the deposit and dissemination of scientific research documents, whether they are published or not. The documents may come from teaching and research institutions in France or abroad, or from public or private research centers.

L'archive ouverte pluridisciplinaire **HAL**, est destinée au dépôt et à la diffusion de documents scientifiques de niveau recherche, publiés ou non, émanant des établissements d'enseignement et de recherche français ou étrangers, des laboratoires publics ou privés.

Persistent luminescence of Eu/Dy-doped $\text{Sr}_2\text{MgSi}_2\text{O}_7$ glass-ceramics processed by aerodynamic levitation

L. Fernández-Rodríguez¹, M. Allix², G. Gorni³, A. Canizarès², S. Ory², G.C. Mather¹, A. Durán¹, D. Levy⁴, M. J. Pascual^{1*}

¹ *Ceramics and Glass Institute (CSIC), Madrid, Spain*

² *CNRS, CEMHTI UPR3079, University of Orléans, F-45071 Orléans, France*

³ *Cells, ALBA Synchrotron Cerdanyola del Vallès, Barcelona, 08290 Spain*

⁴ *Material Science Institute of Madrid (CSIC), Madrid, Spain*

**Corresponding author (mpascual@icv.csic.es)*

Abstract

Glass beads of the $\text{Sr}_2\text{MgSi}_2\text{O}_7$ stoichiometric composition and a non-stoichiometric composition with higher SiO_2/SrO ratio doped with $\text{Eu}_2\text{O}_3/\text{Dy}_2\text{O}_3$ were prepared through aerodynamic levitation coupled to CO_2 laser heating. The glass beads were subsequently treated at 1100 °C to produce glass-ceramics with $\text{Sr}_2\text{MgSi}_2\text{O}_7$: Eu^{2+} , Dy^{3+} as the main crystalline phase. The doped glasses exhibit red emissions; after crystallisation, the corresponding glass-ceramics emit blue light under UV excitation. The starting glass composition considerably affects the crystallisation process, resulting in $\text{Sr}_2\text{MgSi}_2\text{O}_7$ glass-ceramics with very different microstructures which, in turn, have a significant influence on the luminescence properties. The photoluminescence emission spectra of the glass-ceramics under UV light show a broadband emission ($\lambda = 400\text{-}500$ nm) with a main peak assigned to the typical Eu^{2+} transition under excitation at 365 nm. Both the intensity of the emission and the persistence time significantly increase on decreasing temperature. Glass-ceramics from the non-stoichiometric glass composition co-doped with $1\text{Eu}_2\text{O}_3/0.5\text{Dy}_2\text{O}_3$ (mol%.) provided the longest persistence times.

Keywords: $\text{Sr}_2\text{MgSi}_2\text{O}_7$: Eu^{2+} , Dy^{3+} , glass crystallisation, phosphors, glass-ceramics, persistence luminescence, aerodynamic levitation coupled to CO_2 laser heating.

Introduction

Persistent phosphorescent materials can absorb both ultraviolet (UV) and visible light from sunlight and gradually emit energy in the dark at certain wavelengths [1, 2, 3]. In recent years, rare-earth (RE) doped strontium aluminates and silicates [4] have attracted increasing attention due to their persistent luminescence properties, with potential application in optical and scintillation devices, solid-state lasers and radiation detection [5, 6, 7]. Synthesis methods including conventional solid-state reaction [8], chemical routes such as sol-gel [9] and hydrothermal synthesis [10], and less conventional processing methods, such as combustion synthesis [11] or microwave-assisted synthesis [12], have been used to prepare phosphors of different crystalline phases. Nevertheless, the preparation of aluminate and silicate phosphor materials from glass crystallisation has not been widely explored. Solid-state reaction is the most common preparation method and was used by Matsuzawa et al. [1] on synthesising strontium aluminates for the first time. Temperatures of the order of 1900 °C are required to obtain the crystalline phase; in addition, these treatments must be carried out in a reducing atmosphere to reduce the oxidation state of Eu^{3+} to Eu^{2+} and thereby obtain a persistent luminescent material.

Several studies have concluded that co-doping with rare earths promotes the formation of vacancies [13, 14], which may be responsible for increasing the persistence of luminescence. Aitasalo et al. [15] focused on the study of different $\text{MAl}_2\text{O}_4\text{:Eu}^{2+}$ ($\text{M} = \text{Ca}$ and Sr) compounds by solid-state reaction, indicating that the Eu^{2+} brightness was enhanced by codoping with trivalent rare-earth cations. In this mechanism, electrons are excited by thermal energy, which requires the close proximity of vacancies and luminescence centres [16].

Nakanishi et al. [17] obtained SrAl_2O_4 glass-ceramics doped with Eu^{2+} and Dy^{3+} from the $\text{SrO-Al}_2\text{O}_3\text{-B}_2\text{O}_3$ system, using the Frozen Sorbet (FS) method. Commercial powders of SrCO_3 , $\gamma\text{-Al}_2\text{O}_3$, H_3BO_3 , Eu_2O_3 and Dy_2O_3 were used as starting materials and preheated at 1300 °C for 1 hour under a gas flow of 5% H_2 + 95% N_2 in an alumina crucible filled with graphite and protected with a larger alumina crucible to reduce Eu^{3+} to Eu^{2+} . In addition, polycrystalline $\text{SrAl}_2\text{O}_4\text{:Eu}^{2+}$, Dy^{3+} (1 mol% for the Sr site) samples were prepared using a powder sintering method, where the solid-state temperature and reaction time were 1400°C and 6 h, respectively, and the reducing atmosphere was 5% H_2 + 95% N_2 . The single crystal used as a standard was fabricated using an IR imaging

furnace (Cannon machinery Co.). It was found that the SrAl_2O_4 crystals in the glass-ceramics show excellent long-lasting phosphorescence properties and enhanced excitation efficiency at 460 nm in photoluminescence excitation spectra compared to SrAl_2O_4 phosphors prepared by a conventional solid-state reaction. It was suggested that the Al^{3+} sites in the SrAl_2O_4 crystals are partially substituted by B^{3+} .

The decay time in the SrAl_2O_4 glass-ceramic was similar to that of the commercial product (LumiNova/G300M, Nemoto & Co., Ltd.). These results suggested that, for long-term performance, SrAl_2O_4 glass-ceramics prepared by the FS method have some advantages, such as transparency, chemical durability and formability. On arresting the UV irradiation, a persistence of up to 9 min was recorded for the composition $55\text{SrO}-27\text{Al}_2\text{O}_3-18\text{B}_2\text{O}_3-1\text{Eu}_2\text{O}_3-1\text{Dy}_2\text{O}_3$ mol%. In another work, Nakanishi et al. [18] studied a luminescent $\text{SrAl}_2\text{O}_4\text{:Eu,Dy}$ glass-ceramic with high transparency in the visible region, also synthesised using the FS method, with control of the oxygen partial pressure ($p\text{O}_2$) for the oxidation of Eu^{2+} ions. The crystalline phase of the aluminoborate glass-ceramic was composed of well-dispersed SrAl_2O_4 single crystals with Eu^{2+} , Eu^{3+} , and Dy^{3+} ions. The glass-ceramic exhibits a slightly greenish yellow emission and the diffuse transmittance was above 75% at 510 nm. The glass-ceramics with Eu^{2+} , Eu^{3+} and Dy^{3+} ions exhibit multi-emission spectra composed of Eu^{2+} : 4f-5d broadband emission (SrAl_2O_4) and Eu^{3+} and Dy^{3+} : 4f-4f emission (aluminoborate glass). These emission properties lead to a unique phenomenon of colour change in the emission. In emission spectra below 393 nm the 4f-4f transitions of Eu^{3+} and Dy^{3+} ions usually have narrow emission bands; however, the 4f-4f emission bands are evident in the spectra, indicating that Eu^{3+} and Dy^{3+} ions are mainly present in the aluminoborate glass phase. The emission intensity of Eu^{2+} ions in the glass-ceramic depends on the $p\text{O}_2$ during preparation. The largest emission band around 520 nm can be assigned to the 4f-5d transition of Eu^{2+} ions in the SrAl_2O_4 crystalline phase and the maximum emission intensity of SrAl_2O_4 glass ceramics was observed at $p\text{O}_2 = 108$ atm.

The most studied and best known persistent luminescent silicate is $\text{Sr}_2\text{MgSi}_2\text{O}_7\text{:Eu}^{2+}$, Dy^{3+} [8, 19, 20] of the akermanite family, $\text{M}_2\text{MgSi}_2\text{O}_7$ ($\text{M} = \text{Ca}, \text{Sr}$). Nishiura et al. [21] prepared glass-ceramics of the phases $\text{M}_2\text{MgSi}_2\text{O}_7\text{:Eu}^{2+}$ ($\text{M} = \text{Sr}, \text{Ca}$) by first melting the starting materials at 1550 °C in 95% N_2 -5% H_2 . The resulting glass pieces were heat treated under the same reducing atmosphere. The emission observed under an excitation of $\lambda = 396$ nm is associated to the $4f^6 5d^1 \rightarrow 4f^7$ transition of Eu^{2+} . The emission peak wavelengths of the samples shifted from 470 to 530 nm with increasing Ca content,

varying from blue to yellowish-green; however, no persistent luminescence was reported.

None of the above-mentioned investigations determined the $\text{Eu}^{3+}/\text{Eu}^{2+}$ ratio in the studied materials, their distribution in the materials and the relationship of the distribution with the optical properties. However, Wondraczek et al. [22] report glasses prepared in the $\text{MO} - \text{B}_2\text{O}_3 - \text{SiO}_2 - \text{Al}_2\text{O}_3$ ($\text{M} = \text{Mg}, \text{Ca}$ and Sr) system with $\text{SiO}_2 \leq 40\%$ molar, and doped with Eu_2O_3 using glucose as a reducing agent in the melting process. Ground powder and bulk samples were prepared from the obtained glass, then transformed into glass-ceramics by heat treatment in air. To evaluate the main crystallisation mechanism, the bulk samples were compared with the powder samples by Differential Scanning Calorimetry (DSC). The absence of an exothermic crystallisation peak in the scan of the bulk sample clearly indicates that crystallisation occurs by surface nucleation. The emission from the glass shows a characteristic Eu^{3+} (red) band, while the glass-ceramic emits with Eu^{2+} (blue). Scanning electron microscopy-cathode-luminescence (SEM-CL) characterisation indicated that the crystalline phase is associated with Eu^{2+} dominant emission, and it is proposed that Eu^{2+} is incorporated in the Sr^{2+} sites of the akermanite structure, while Eu^{3+} accumulates in the intergranular phase of the glass.

Aerodynamic-levitation (ADL) coupled to laser heating is one of the most widely used contactless solidification methods for efficient bulk-glass manufacture, in which the sample is levitated by gas and melted by CO_2 laser irradiation. The method avoids heterogeneous nucleation, preventing contamination from the container, and promotes the formation of deep subcooling melts. The cooling rate depends on the size of the bead (usually limited to about 3 mm in diameter) and the nature of the gas used. In addition, high temperatures (almost 3000 °C) can be reached with this technique [23, 24, 25, 26]. Hence, new glasses that cannot be obtained by conventional methods may be manufactured.

Shinozaki et al. [27] synthesised hexagonal $\text{SrAl}_2\text{O}_4:\text{Eu}^{2+}, \text{Dy}^{3+}$ crystals via a levitation-melting technique, first obtaining precursor glass beads which were crystallised on heat treatment at 1000 °C for 1 hour in H_2 . The crystallised and solidified supercooled glass showed a broad excitation peak in the range of $\lambda=300\text{-}500$ nm. The photoluminescence emission spectra and decay curves indicated that all samples exhibited excellent afterglow, with emission intensity greatest for the solidified supercooled melt, followed by the crystallised glass, then the ceramics prepared by solid-state reaction.

Fernández-Carrion et al. [24] also investigated three glass compositions $\text{Sr}_{1-x/2}\text{Al}_{2-x}\text{Si}_x\text{O}_4$ ($x = 0.2, 0.4$ and 0.5) doped with Eu prepared by the levitation method. The glasses were heat treated in an open atmosphere furnace to induce complete crystallisation of the glass. The glass-ceramic emitted red or blue light after excitation at 254 or 365 nm, respectively. Interestingly, the ratio between the Eu^{2+} and Eu^{3+} emission bands can be adapted depending on the excitation wavelength, resulting in different emission colours. In a deeper investigation of the same glass phase, $\text{Sr}_{1-x/2}\text{Al}_{2-x}\text{Si}_x\text{O}_4$, Fernández-Carrion et al. [28] observed that the glass-ceramics show a colour change varying from green to light blue in both photoluminescence and persistent luminescence measurements. This colour change is assigned to a blue shift of the Eu^{2+} $5d \rightarrow 4f$ emission and the appearance of Dy^{3+} emission lines. In addition, it was also observed that materials with increasing Si contents show longer persistent decays.

We previously reported Eu/Dy-doped $\text{Sr}_2\text{MgSi}_2\text{O}_7$ glass-ceramics showing persistent blue emission lasting a few minutes, which were prepared from sintering and crystallisation of glass powders in an oxidising atmosphere employing a glass composition with higher SiO_2/SrO ratio than the stoichiometric composition [29]. Attempts were also made to melt the glass with the $\text{Sr}_2\text{MgSi}_2\text{O}_7$ stoichiometric composition at 1780 °C and fast cooling rates, but crystallised samples containing $\text{Sr}_3\text{MgSi}_2\text{O}_8$ were obtained after cooling, suggesting that much higher temperatures combined with much faster cooling are required to prepare the stoichiometric glass composition.

In the present study, aerodynamic levitation is used to synthesise glasses that cannot be melted in a conventional electric or gas furnace due to temperature limitations. In particular, glass beads of the $\text{Sr}_2\text{MgSi}_2\text{O}_7$ stoichiometric composition and a non-stoichiometric composition with higher SiO_2/SrO ratio doped with $\text{Eu}_2\text{O}_3/\text{Dy}_2\text{O}_3$ were prepared through aerodynamic levitation coupled to CO_2 laser heating. As previously described, only the non-stoichiometric composition could also be melted by conventional furnace. The crystallisation behaviour of the glass beads will be studied and the luminescent properties of the final glass-ceramics will be discussed, taking into account their structural properties. The glasses and corresponding glass-ceramics are characterised by thermal and structural techniques and the optical characterisation involves measurement of the photoluminescence (PL) and persistence properties at different temperatures.

2. Experimental procedure

2.1. Materials preparation

Undoped and $\text{Eu}_2\text{O}_3/\text{Dy}_2\text{O}_3$ co-doped glasses of the stoichiometric $\text{Sr}_2\text{MgSi}_2\text{O}_7$ composition (40 SiO_2 -40 SrO -20 MgO mol%, labelled hereafter as Ls) and a non-stoichiometric composition with a higher SiO_2/SrO ratio (55 SiO_2 -27 SrO -18 MgO mol%, labelled L) were prepared using CO_2 laser-heating coupled to an aerodynamic levitation system. The labels of the prepared doped glasses for the stoichiometric (Ls) and non-stoichiometric (L) compositions are followed by the amount of added dopant in mol% (Ls-0.5Eu, Ls-1Eu-0.5Dy, L-0.5Eu, L-1Eu-0.5Dy).

The precursor materials of SiO_2 sand (Saint-Gobain, 99.6%), SrCO_3 (Alfa Aesar, 97.5%), MgO (PanReac, 98%), Eu_2O_3 (Alfa Aesar, >99.9%) and Dy_2O_3 (Alfa Aesar, >99.9%) were weighed (1.5g batch) and milled together in ethanol using an agate mortar to ensure homogeneity. The powder mixtures were then pressed into pellets (\varnothing = 13 mm, h = 2 mm), a small portion of which was placed on a metallic nozzle and levitated by an argon flow; upper and lower CO_2 laser beams ensured homogeneous heating and melting. When the sample is levitating, it is heated to fusion and the temperature is measured by infrared pyrometry. Stoichiometric and non-stoichiometric compositions were heated to $\sim 2400^\circ\text{C}$ and 1600°C , respectively, achieving homogenisation for a few seconds before the laser was quickly switched off. Glass beads were obtained by free-cooling of the high temperature liquid under contactless conditions after shutting off the lasers.

The glass beads were further heat treated in an electric furnace at 1100°C for 1 min (10 $^\circ\text{C}/\text{min}$ heating and cooling rates) in air or a 90% N_2 /10% H_2 atmosphere to obtain the corresponding glass-ceramic materials. Samples prepared in a reducing atmosphere include "-red" at the end of the label. A total of nine samples have been studied and listed in table 1.

Table 1. Glass compositions (mol%.) and atmospheres used for the crystallization thermal treatment.

Sample name	SiO ₂	Sr ₂ O	MgO	Eu ₂ O ₃	Dy ₂ O ₃	Atmosphere
Ls-0.5Eu	39.80	39.80	19.90	0.50	-	air
Ls-0.5Eu-red	39.80	39.80	19.90	0.50	-	90%N ₂ /10%H ₂
Ls-1Eu-0.5Dy	39.42	39.41	19.70	0.99	0.49	air
Ls-1Eu-0.5Dy-red	39.42	39.41	19.70	0.99	0.49	90%N ₂ /10%H ₂
L-undoped	55	27	18	-	-	air
L-0.5Eu	54.73	26.86	17.91	0.50	-	air
L-0.5Eu-red	54.73	26.86	17.91	0.50	-	90%N ₂ /10%H ₂
L-1Eu-0.5Dy	54.19	26.60	17.73	0.99	0.49	air
L-1Eu-0.5Dy-red	54.19	26.60	17.73	0.99	0.49	90%N ₂ /10%H ₂

2.2. Thermal and structural characterisation

The glass-bead samples were milled (particle size < 40 µm) in an agate mortar and analysed by differential scanning calorimetry (DSC) using a Setaram multi HTC 96 instrument. Measurements were performed on 200 mg of glass powder placed in a platinum-rhodium crucible and heated to 1200 °C with a heating rate of 10 °C/min under an argon gas flow (20 ml/min) to determine the temperatures of glass-transition (T_g), initiation of crystallisation (T_x) and crystallisation (T_c).

DTA curves were recorded with an SETARAM Setsys Evolution instrument, using samples of particle size < 20 µm up to 1200°C with 10 °C/min heating rate.

In-situ high temperature X-ray diffraction data were collected during isothermal steps in the range 600-1200 °C on a D8 Advance Bruker diffractometer (CuK $\alpha_{1,2}$ radiation) equipped with a Vantec-1 linear detector operating over the range $15 \leq 2\theta \leq 70^\circ$ with a 0.024° step size (total duration of 20 minutes per scan). A HTK1200N Anton Paar oven chamber based on a Kanthal® resistive heating attachment heated the milled glass powders, which were placed in a corundum crucible covered with a platinum foil. In addition, room temperature XRD patterns of glass-ceramic beads, milled and sieved to a particle size lower than 60 µm, were collected on a (Bruker D8 Advance) in the range $15 \leq 2\theta \leq 70^\circ$ with a step size of 0.02 °, employing CuK α_1 radiation ($\lambda=1.54056 \text{ \AA}$).

In-situ Raman measurements of the L-1Eu-0.5Dy sample were performed on a Renishaw InVia Qontor spectrometer. Room-temperature reference spectra were acquired at various wavelength (355, 488 and 514 nm) for glass and crystalline samples (grating 1800 gr.mm⁻¹, 50x - 0.8 NA microscope objective). For temperature analysis, to avoid thermal emission, a UV configuration was chosen (355 nm laser, 3600 gr/mm grating and 15x – 0.3 NA long working distance microscope objective).

Raman measurements of the L-1Eu-0.5Dy, Ls-1Eu-0.5Dy and Ls-0.5Eu glass-ceramic surfaces were carried out on an InVia Raman spectrometer (Renishaw plc, UK) equipped with a 514 nm Ar⁺ laser and a 50× magnification objective.

X-ray absorption spectroscopy (XAS) was performed at the CLAES beamline at the ALBA Synchrotron (Spain) [30]. The incident energy was monochromatised by a double crystal monochromator Si(311) cooled with liquid nitrogen. The rejection of higher harmonics was achieved by a combination of coating and angle of collimating and focusing mirrors. The beam size at the sample position was adjusted to ~ 300 µm × 300 µm. The samples (8 beads of glass/glass-ceramic powder) were pressed into 5 mm diameter pellets and the spectra at the Eu L₃- and Dy L₂-edges were measured in fluorescence mode using a six-channel silicon drift detector (RaySpec with Xspress'3 from Quantum Detector). The choice of measuring the samples in fluorescence mode was taken after checking the chemical composition and calculating the absorption jump at the Eu L₃ and Dy L₂-edges. Fluorescence mode is a better detection method compared to transmission when the jump is below 0.1. In fluorescence mode, the incident flux and the fluorescence X-rays (L_α and L_β emission lines for Eu and Dy, respectively) are measured. The fluorescence detector was set at 90° to the incident beam direction and the samples placed at 45°. Appropriate amounts of Eu₂O₃, EuF₂ and Dy₂O₃ powder were weighted to have an absorption jump around 1, then mixed with cellulose and finally pressed into pellets and measured in transmission mode. The incident and transmitted intensity were detected using two ionisation chambers filled to 1 bar with a mixture of N₂/He and N₂/Kr to achieve 10 and 75 % of absorption, respectively. Six to twelve scans were required in fluorescence mode to increase the signal-to-noise ratio, whereas four spectra were acquired in transmission mode. Data analysis was carried out using the ATHENA and ARTEMIS software of the DEMETER package [31]. The spectra measured in fluorescence mode were corrected for self-absorption using the FLUO algorithm [32].

Scanning Electron Microscopy-Cathode luminescence (SEM-CL) was performed on a Hitachi S-3000 N microscope equipped with a vacuum chamber, on excitation with an electron beam of voltage 15–25 kV and a filament intensity of 100 μA . The emission spectra were recorded employing a fibre spectrometer with a charge-coupled device (CCD) through an optical fibre, and the corresponding luminescence photographs with an ordinary camera. The instrument is equipped with secondary electron (SE) and backscattered electron (BSE) detectors, an energy dispersive X-ray spectroscopy (EDX) Quantax (model XFlash 6I30, Bruker) and a cathode-luminescence system (CHROMA-CL2 Gatan). Samples were compositionally accurate to within the uncertainty in the EDX measurement ($\sim 1\%$). Additionally, spectrally resolved CL measurements were carried out at 80 K on a MONO-CL2 system (Gatan) attached to a Field Emission Scanning Electron Microscope (FE-SEM, ZeissLEO 1530). Detection is performed with a photomultiplier for panchromatic images, and a Peltier cooled Si-CCD for spectrally resolved images.

2.3. Optical properties

The glass-ceramic pellets were observed under UV light (18W ($\lambda = 365\text{ nm}$), $I = 0.025\text{ mA / cm}^2$) at room temperature in a dark room and with a stopwatch in hand to check the emission and persistence of phosphorescence. The persistence values are approximate because there is human error. To give more accurate values, the experiment was repeated several times. Fluorometric measurements of the glass-ceramic samples were performed at room temperature using an Avantes spectrometer (AvaSpec-ULS2048L) attached to an Ultra-Low Straylight Fiber Optic VIS/NIR Slit 25-RS spectrometer. A front-surface sample holder was used for data collection and oriented at 60 degrees to the angle of light excitation to minimise scattered light. Appropriate filters were used to eliminate Rayleigh and Raman scatter from the emission. Emission spectra were corrected for the wavelength dependence of the 150-Watt Xenon arc excitation, but not for the wavelength dependence of the detection system.

Lifetime measurements were measured using an AvaSpec-ULS2048CL-EVO-RS with a CMOS detector operating at an integration time of 150 ms and averaging 3 spectra. A water-cooled cryostat was integrated in the isolated sample chamber to enable temperature-dependent lifetime measurement. The temperature was measured by a PT100 sensor placed as close as possible to the sample with an accuracy of $\pm 1^\circ\text{C}$.

3. Results and discussion

All doped glass beads show red emission under UV exposure ($\lambda = 365$ nm), figure 1c. Figures 1 a and b show typical images of glass and glass-ceramic beads (L-1Eu-0.5Dy), respectively. Under UV light, glass-ceramic beads showed a bright blue luminescence. Once the UV lamp is turned off, the blue emission is persistent in some of the samples, such as L-1Eu-0.5Dy (figure 1d). Table 2 lists the blue persistence time measured with the naked eye for all samples studied at room temperature and 0 °C. The persistence time increases significantly with decreasing temperature, with L-1Eu-0.5Dy showing the highest persistence. This was also the case for sample G-1Eu-0.5Dy of the same composition melted in a gas furnace, as described in our previous research [29].

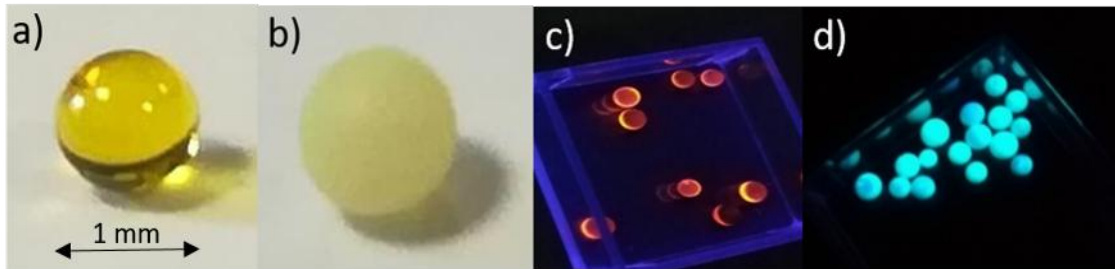


Figure 1. Image of a) glass bead in daylight, b) glass-ceramic bead in daylight c) red emission from glass beads under UV lamp (365 nm) and d) persistent blue luminescence of glass-ceramic beads (UV lamp off). Composition: L-1Eu-0.5Dy.

Table 2. Duration of persistent blue emission from glass-ceramics under excitation at 365 nm observed with the naked eye (NP, no persistence).

Sample	Persistent blue emission at RT (s) \pm 1	Persistent blue emission at 0° C (s) \pm 1
Ls-0.5Eu	NP	NP
Ls-0.5Eu-red	NP	NP
Ls-1Eu-0.5Dy	10	13
Ls-1Eu-0.5Dy-red	11	15
L-0.5Eu	15	19
L-0.5Eu-red	12	16
L-1Eu-0.5Dy	41	82
L-1Eu-0.5Dy-red	24	47

Based on these results, we will focus on the characterisation of the L-1Eu-0.5Dy and L-undoped glass-ceramics, from which the largest amount of sample (beads) was

obtained. Although, complementary characterisation of the other glass-ceramics is also provided for comparison purposes, it has not been possible to perform a complete thermal and structural analysis due to the limited amount of sample.

3.1. Thermal and structural properties

Figure 2 shows the DSC curves for the L-undoped and L-1Eu-0.5Dy glass compositions. The L-undoped glass shows a glass transition temperature (T_g) around 742 °C and an exothermic peak (T_c) at ~ 980 °C, attributed to the crystallisation process. DSC analysis of the L-1Eu-0.5Dy glass shows the same crystallisation peak, but it is wider, flatter and shifted to a slightly lower temperature; T_g for both samples is similar. The broader crystallisation peak for the L-1Eu-0.5Dy sample arises from a lower onset of crystallisation (T_x) compared to the L-undoped sample and the possible crystallisation of several different phases. At temperatures higher than 1100 °C, there is an endothermic peak associated with the melting of the crystalline phase.

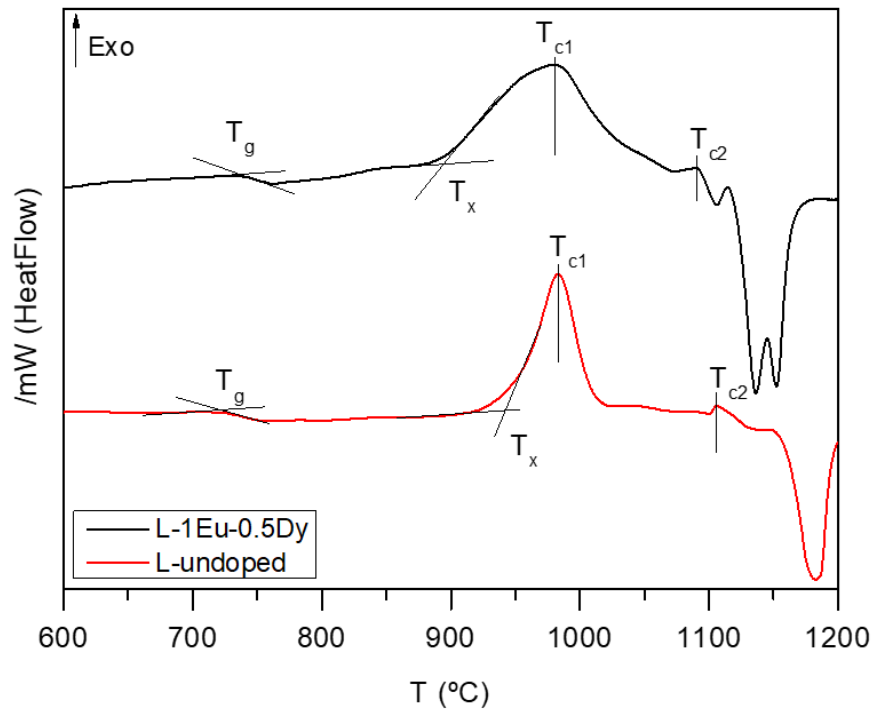


Figure 2. DSC curves of the L-undoped and L-1Eu-0.5Dy compositions (heating rate, 10 °C/min).

Figure A.1 shows the DTA of the Ls-1Eu-0.5Dy sample, particle size < 40 μm . The T_g appears at $\sim 750 \pm 2$ $^{\circ}\text{C}$, in addition to two main crystallisation peaks at 897 and 908 $^{\circ}\text{C}$. Crystallisation for the Ls-1Eu-0.5Dy sample occurs about 90 $^{\circ}\text{C}$ earlier than for L-1Eu-0.5Dy. For the sample Ls-1E-0.5Dy since in the ATD crystallization peaks were obtained around 900 $^{\circ}\text{C}$, the glass was heat treated to obtain the glass-ceramic at that temperature, but the result was a predominant of the $\text{Sr}_3\text{MgSi}_2\text{O}_8$ crystalline phase, therefore the final heat treatment was at 1100 $^{\circ}\text{C}$, as the rest of the samples, obtaining mostly the $\text{Sr}_2\text{MgSi}_2\text{O}_7$ crystalline phase.

Table 3. T_g , T_x and T_c ($^{\circ}\text{C}$) of L glasses.

	$T_g (\pm 2)$	$T_x (\pm 2)$	$T_{c1} (\pm 2)$	$T_{c2} (\pm 2)$
L-Undoped	742	927	983	1100
L-1Eu-0.5Dy	748	893	980	1090

In-situ high temperature XRD of the L-undoped glass, Figure A.2, reveals that for the $\text{Sr}_2\text{MgSi}_2\text{O}_7$ phase (ICDD: 75-1736) the first peaks of crystallisation start to appear at 850 $^{\circ}\text{C}$. Other secondary phases are also present, such as SrSiO_3 , SiO_2 and a non-identified phase once 1100 $^{\circ}\text{C}$ is reached. The XRD pattern of L-1Eu-0.5Dy treated at 1100 $^{\circ}\text{C}$ for one minute (figure 3a) indicates $\text{Sr}_2\text{MgSi}_2\text{O}_7$ as the main phase but with a considerable amount of secondary phase which matches with the ICDD pattern of metastable SrSiO_3 of undetermined structure (032-1257) [33]. Further peaks were attributed to phases present in lesser quantity, including low quartz (13-0026) and SrCO_3 (05-0016). A number of other peaks were unable to be identified despite exhaustive searches in the Inorganic Crystal Structure Database (ICSD) and the International Centre for Diffraction Data (ICDD) database.

For the Ls-1E-0.5Dy sample (figure 3b), the main phases are $\text{Sr}_2\text{MgSi}_2\text{O}_7$ (akermanite) and $\text{Sr}_3\text{MgSi}_2\text{O}_8$. The latter phase also crystallised on cooling the glass composition 40 SiO_2 -40 SrO -20 MgO which was melted in a conventional electric furnace. The appearance of $\text{Sr}_3\text{MgSi}_2\text{O}_8$ may be expected on consideration of the equilibrium phase diagram [34]. An undetermined phase was also discerned in the XRD pattern. The refinement fit of Ls-1E-0.5Dy is shown in figure A.3. Cell parameters of $\text{Sr}_2\text{MgSi}_2\text{O}_7$ ($a = 8.0077(8)$; $c = 5.1619(6)$ \AA) and $\text{Sr}_3\text{MgSi}_2\text{O}_8$ ($a = 9.448(1)$, $b = 5.4461(9)$, $c =$

13.882(2) Å) were refined in space groups $C2/c$ and $P2_1/c$, respectively, based on published structural data [35, 36] with the Fullprof program using pseudo-Voigt profile functions and interpolation of background points. Refined quantities of 68 and 32 wt% were determined for the ratios of crystallised $Sr_2MgSi_2O_7$ and $Sr_3MgSi_2O_8$, respectively. A full quantitative analysis also accounting for the residual glassy phase was not performed due to the presence of an unidentified minor phase.

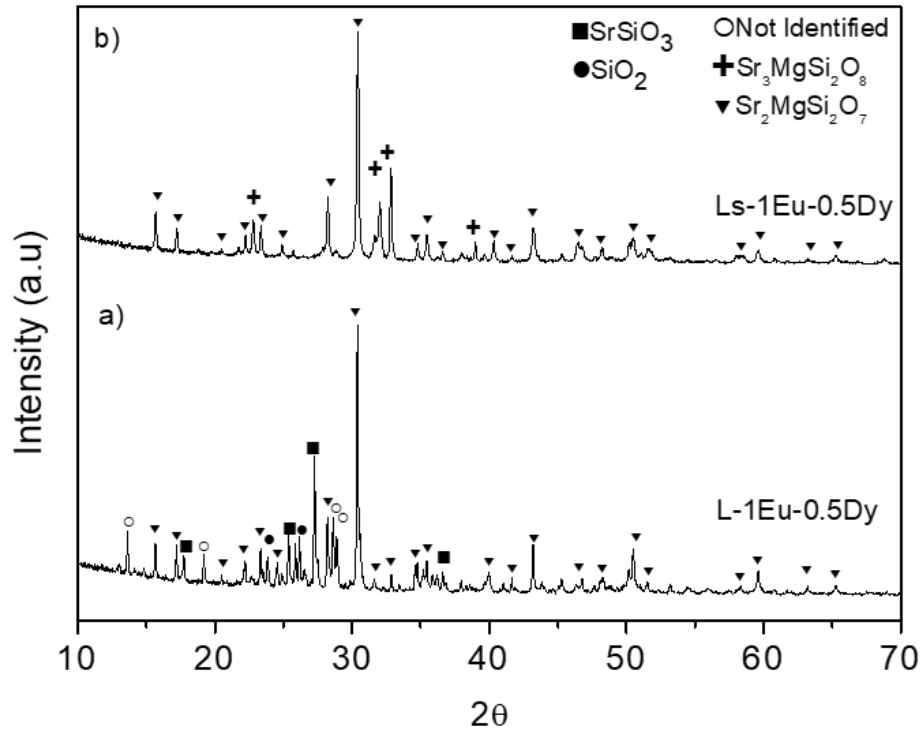


Figure 3. XRD patterns of glass-ceramic samples a) L-1Eu-0.5Dy and b) Ls-1Eu-0.5Dy.

Figure 4 shows the high-temperature, in-situ Raman spectra of L-1Eu-0.5Dy, which confirms that $Sr_2MgSi_2O_7$ starts to crystallise at 960 °C with its typical Raman spectrum obtained at 1100 °C. The most intense and sharp Raman lines in the in-situ spectrum are observed at 315, 448, 630, 882 and 957 cm^{-1} . Compared to previous studies of the same phase, Hanuza et al. [37] assigned the bands to the corresponding modes: asymmetric bending $\delta_{as}(Si^{\circ}Si)$, 985 cm^{-1} ; symmetric stretching $\nu_s(SiO_3)$, 901 cm^{-1} ; symmetric stretching, $\nu_s(Si^{\circ}Si)+\nu_s(SiO_3)$, 652 cm^{-1} ; asymmetric bending $\delta_{as}(SiO_3)$, 450 cm^{-1} ; and bending $\delta(Si^{\circ}Si)$, 316 cm^{-1} . The main modes are similar to those in the literature but

with a small shift, which is due to the temperature distortion of the structure and harmonicity. When performing the Raman spectrum of the sample once it has returned to room temperature, the main peaks coincide exactly with those obtained in the literature.

Figure A.4 shows the Raman spectra of the glass-ceramics L-1Eu-0.5Dy, Ls-1Eu-0.5Dy and Ls-0.5Eu, in which only the $\text{Sr}_2\text{MgSi}_2\text{O}_7$ phase is detected [37]. This is also the case for most of the glass-ceramic samples. The Raman spectra of the glass-ceramic Ls-0.5Eu exhibited several other peaks, in addition to those of the $\text{Sr}_2\text{MgSi}_2\text{O}_7$ phase. Three of the main peaks, 381, 568 and 995 cm^{-1} , appearing in the Raman spectra are associated with the $\text{Sr}_3\text{MgSi}_2\text{O}_8$ phase [38] observed by XRD.

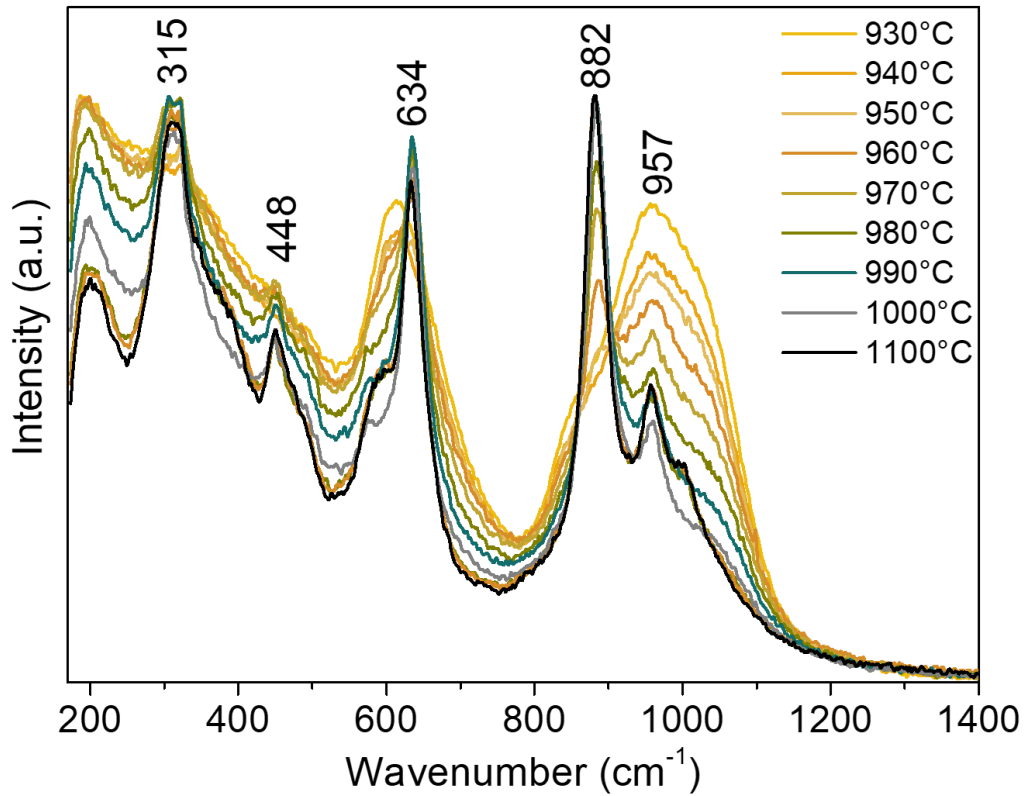


Figure 4. In-situ Raman spectra of the L-1Eu-0.5Dy sample.

Figure 5a shows the SEM image of the surface of a crystallised L-1Eu-0.5Dy bead, in which white crystals (point 1), grey crystals (point 2) and, in a much smaller amount, black areas (point 3) are all embedded in a rather reduced residual glassy phase. The composition of each point is listed in Table 4. SEM analysis of the cut and polished

beads was also performed, but it was found that crystallization is mainly superficial and decreasing from the inside out as can be seen in figure A.5.

An EDX analysis was performed, but considering that the size of the crystals is small and the spot size of the equipment is large, the results obtained are semi-quantitative. The analysis is useful for comparing the different microstructures of the samples, but does not reflect the real compositional values, particularly for the dopant content. The grey crystals, point 2, correspond to the $\text{Sr}_2\text{MgSi}_2\text{O}_7$ phase; no Eu/Dy (1/0.5 mol %) incorporation in the akermanite phase could be quantified by EDX. Point 1 corresponds to a phase rich in SiO_2 and SrO with no MgO , in which Eu_2O_3 and Dy_2O_3 seem to concentrate. Hence, this phase may correspond to metastable SrSiO_3 observed in the X-ray diffractograms. It may instead match in composition with the SrSi_2O_5 phase; however, after searching in the ICDD and ICSD databases, only the structure of a high-pressure SrSi_2O_5 phase [39] was found, the XRD pattern of which does not coincide with any diffraction peak of the pattern shown in Figure 3a. Point 3 (black zones) is very rich in SiO_2 and is likely attributable to residual glassy phase.

Elemental mapping of the glass-ceramic, presented Figure 5b, reveals that europium and dysprosium are concentrated in the white crystals, whereas magnesium is absent. In the darker grey crystals, the elements corresponding to the akermanite phase, strontium, silicon and magnesium are clearly found. The cathodoluminescence images of L-1Eu-0.5Dy (Figure 5c) indicate that the green emission emanates from the grey microcrystals ($\text{Sr}_2\text{MgSi}_2\text{O}_7$ phase), whereas the residual glassy phase remains dark.

Figure 5d shows SEM images of the crystallised Ls-1Eu-0.5Dy bead surface; the corresponding EDX analysis is provided in Table 4. There is a small distribution of white areas (point 1) where the rare earths seems accumulate. The grey crystals, point 2, correspond to the $\text{Sr}_2\text{MgSi}_2\text{O}_7$ phase, in which incorporation of Eu/Dy can be detected.

It is observed that the $\text{Sr}_2\text{MgSi}_2\text{O}_7$ microcrystals are larger (8-16 μm) in the L-1Eu-0.5Dy glass-ceramics compared to the Ls-1Eu-0.5Dy glass-ceramics (1-3 μm). Additionally, almost no residual glassy phase is observed in the Ls glass-ceramic. Therefore, as expected, the difference in composition of the starting glasses strongly affects the nucleation and growth of the optically active crystals under the same thermal treatment. Although there is green contrast, the cathodoluminescence image of the Ls-1Eu-0.5Dy glass-ceramic, Figure 5e, reveals that the emission originates from all the microcrystals.

The EDX results shown in table 4 demonstrate that the akermanite phase corresponds to the phase responsible for the strong emission observed by cathodoluminescence.

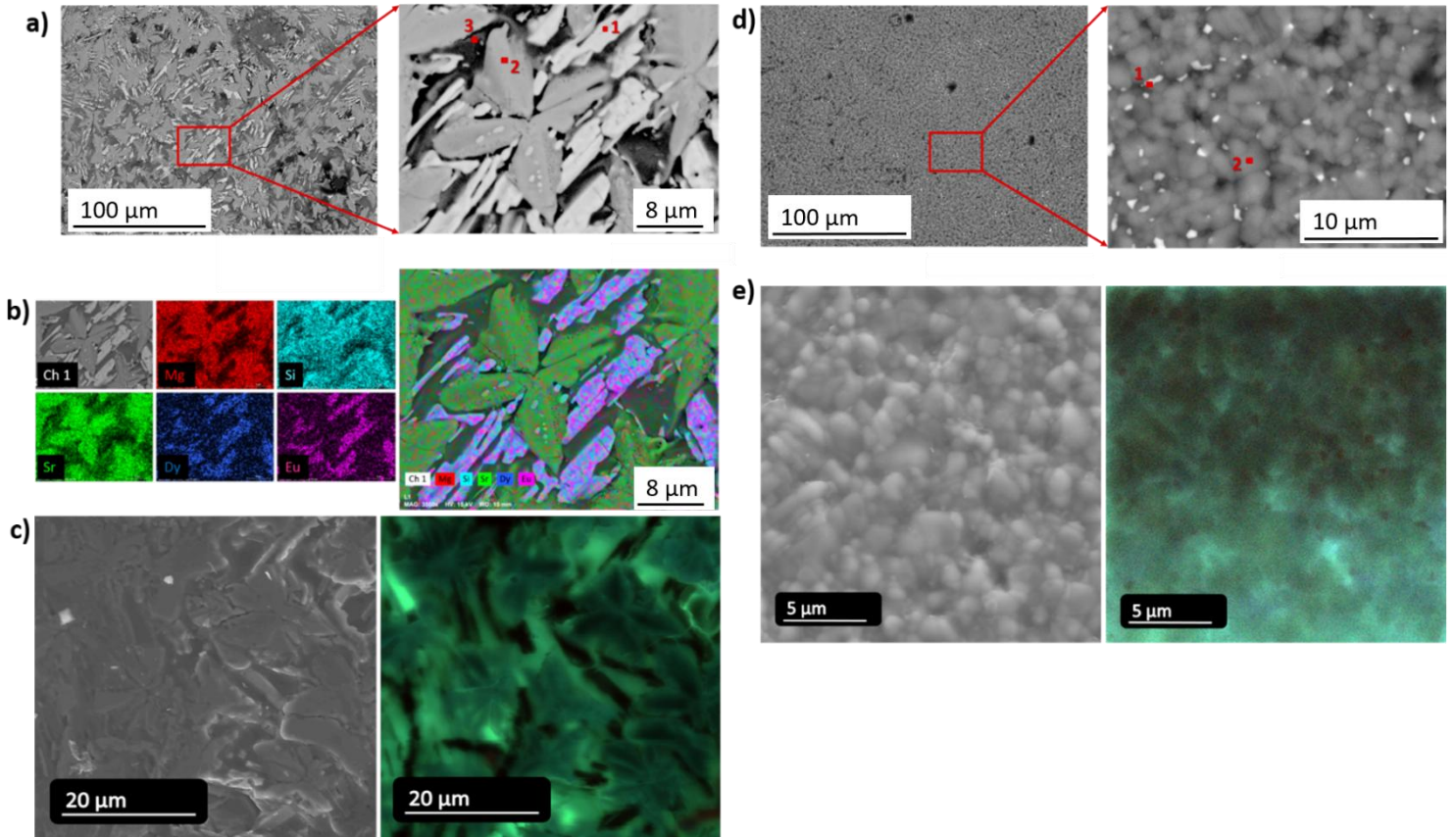


Figure 5. a) SEM image of the L-1Eu-0.5Dy glass-ceramic and b) elemental mapping of the L-1Eu-0.5Dy glass-ceramic, c) SEM-CL images of the surface of sample L-1Eu-0.5Dy, d) SEM images of the surface of Ls-1Eu-0.5Dy glass-ceramic and e) SEM-CL images of the surface of sample Ls-1Eu-0.5Dy.

Table 4. EDX compositional analysis (mol %) of the L-1Eu-0.5Dy glass-ceramic corresponding to the points 1, 2 and 3 in Figure 5a, and of Ls-1Eu-0.5Dy glass-ceramic corresponding to the points 1 and 3 in Figure 5d. The initial nominal glass composition is also shown.

L-1Eu-0.5Dy				
	Nominal glass composition	1	2 Sr ₂ MgSi ₂ O ₇	3
SiO ₂	54.2	61.6	39.9	61.0
SrO	26.6	30.8	41.1	21.4
MgO	17.7	-	19.9	17.0
Eu ₂ O ₃	1.0	5.0	-	-
Dy ₂ O ₃	0.5	2.7	-	-
Ls-1Eu-0.5Dy				
	Nominal glass composition	1	2 Sr ₂ MgSi ₂ O ₇	
SiO ₂	39.4	36.1	34.1	
SrO	39.4	45.0	42.8	
MgO	19.7	12.9	21.5	
Eu ₂ O ₃	1.0	4.1	1.2	
Dy ₂ O ₃	0.5	1.8	0.5	

Figure 6 shows the X-ray absorption near edge structure (XANES) of L-1Eu-0.5Dy glass and the corresponding glass-ceramics obtained in air and in a reducing atmosphere, in addition to the XANES spectra for the Ls-1Eu-0.5Dy glass-ceramic crystallised in air. The majority of Eu ions are present as Eu³⁺, as confirmed by the edge-energy value of the whiteline position around 6980 eV, associated with the 2p-5d transition in Eu₂O₃. The high sensitivity of the technique (~ 1 ppm) allows the detection of small but readily discernible amounts of Eu²⁺. A resonance at ~ 6975 eV is observed in all samples, corresponding with the whiteline position of Eu²⁺ ions, as confirmed by the EuF₂ reference spectrum. The quantification of Eu³⁺ and Eu²⁺ was performed using a peak- fitting procedure described in detail elsewhere [40]. The transition to the continuum is modelled by an arctan function and the whitelines of Eu²⁺ and Eu³⁺ are fitted using pseudo-Voigt profile shapes. The fits are shown in figure A.6 and the results of the fit are summarised in Table 5.

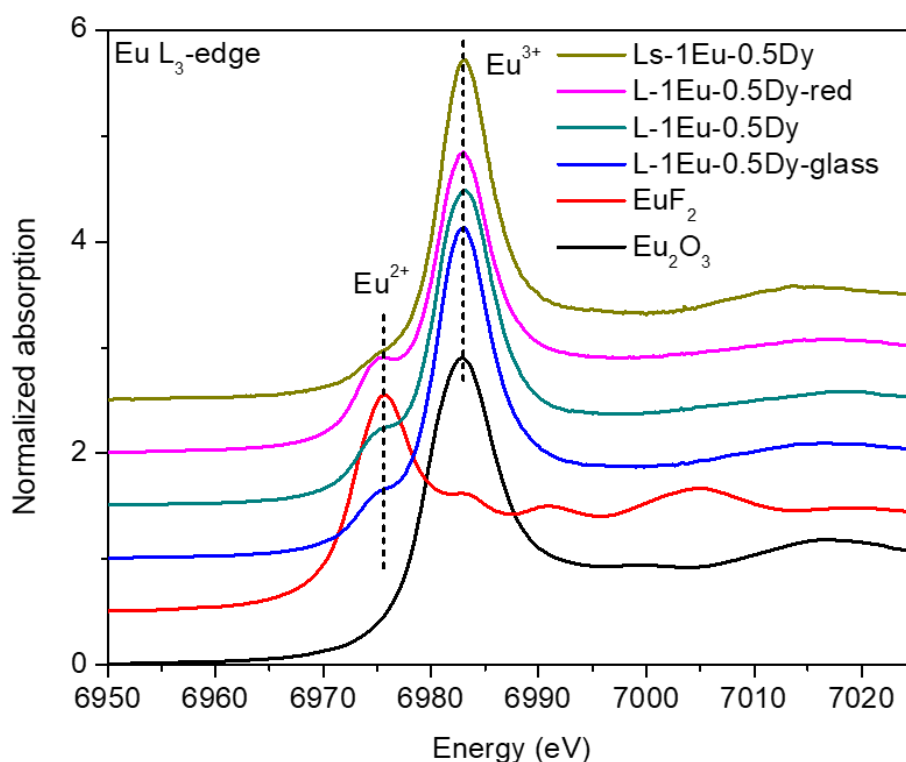


Figure 6. Normalised XANES spectra at the Eu L₃-edge of samples and references.

Table 5. Eu³⁺/Eu²⁺ ratio obtained from the peak-fitting procedure (error around 2%).

Sample	Eu ³⁺ (%)	Eu ²⁺ (%)	R-factor
L-1Eu-0.5Dy glass	88	12	0.0005
L-1Eu-0.5Dy	85	15	0.0002
L-1Eu-0.5Dy -red	82	18	0.0003
Ls-1Eu-0.5Dy	94	6	0.0002

The fraction of Eu²⁺ is around 12% in the L-1Eu-0.5Dy-glass, increasing to 15% when the glass is crystallised in air and up to 18% in a reducing atmosphere. In contrast, the fraction of Eu²⁺ ions in the Ls-1Eu-0.5Dy is much less, ~ 6%. Figure 7 shows the first shell fit of the Extended X-ray absorption fine structure (EXAFS), which mostly provides information on the local structure around Eu³⁺ ions considering their much higher content. The results, summarised in Table A.1, indicate a similar local environment for the L-1Eu-0.5Dy glass and the L-1Eu-0.5Dy glass-ceramic treated in air, in addition to a relatively disordered environment around the Eu³⁺ ions (estimated by the σ^2 parameter). This could be an indication of the presence of Eu³⁺ in the residual

glassy phase or other disordered environment, such as the grain boundary, as observed in other samples using cathodoluminescence [29].

There is a noticeable decrease of the amplitude of the first shell after heat treatment in a reducing atmosphere. This could be related to the slight increase of the Eu^{2+} content ($\sim 20\%$) which reduces the amplitude of the oscillations by destructive interference, as described in detail in a previous work [40]. Another possibility is that the increasing vacancy content during heat treatment in reducing atmosphere induces structural disorder around the Eu^{3+} ions. The bond distance and disorder parameter of the Ls-1Eu-0.5Dy sample are similar, within error, to those of L-1Eu-0.5Dy glass-ceramic treated in air.

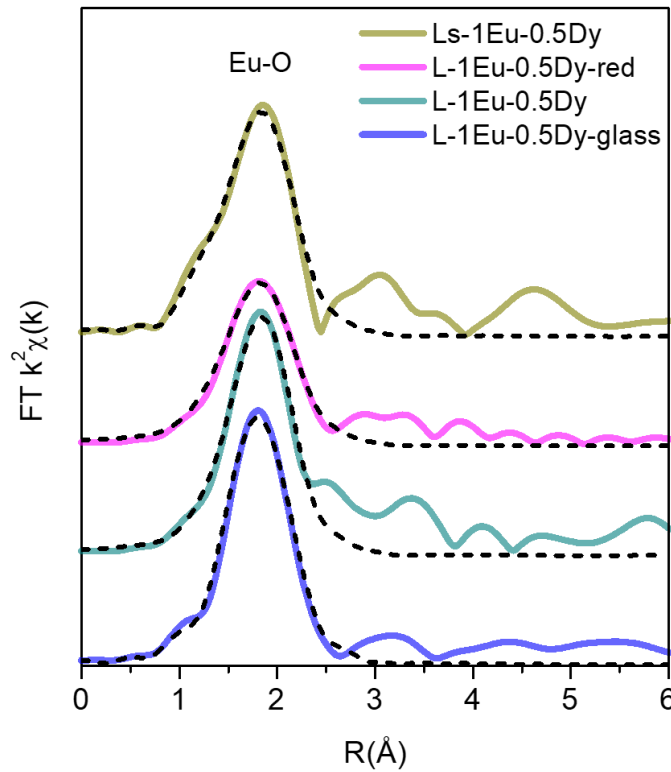


Figure 7. Fourier Transform (FT) of $k^2\chi(k)$ spectra (solid line) at the Eu L_3 -edge and corresponding first-shell fit (dashed line).

Figure 8 shows the XANES spectra at the Dy L_2 -edge, together with the Dy_2O_3 reference. The measurements were performed at the L_2 -edge to avoid overlap between the Eu L_1 -edge (8052 eV) and the Dy L_3 -edge (7790 eV). The edge position at 8985 eV

and the whiteline at 8987 eV indicate the presence of only Dy^{3+} ions in static conditions, that is, without illuminating the system with UV light. Other authors have reported the formation of metastable Eu^{3+} - Dy^{2+} centres on irradiation with UV light in Eu/Dy co-doped $\text{Sr}_4\text{Al}_{14}\text{O}_{25}$ phosphors [41].

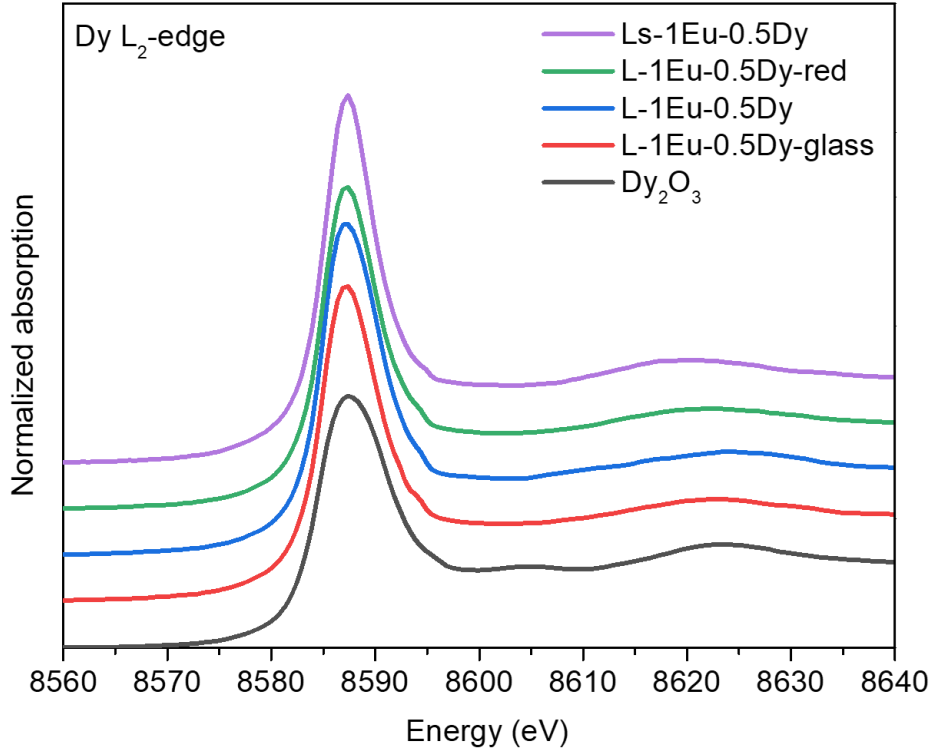


Figure 8. Normalised XANES spectra at the Dy L_2 -edge of studied samples and Dy_2O_3 reference.

Figure 9 shows the first shell fit of the EXAFS spectrum at the Dy L_2 -edge. There is an increase in the amplitude of the first shell for the glass-ceramic prepared in air, whereas the intensity of the first shell decreases when crystallisation occurs in a reducing atmosphere, table A.2. This behaviour indicates the change from a relatively disordered environment in the glass to a more regular one in the glass-ceramic sample, associated with the incorporation of Dy^{3+} in the crystal phase, as confirmed by EDX analysis (figure 4). However, after heat treatment in the reducing atmosphere, the noticeable decrease of the shell amplitude is associated with greater disorder, most likely due to the creation of vacancies, as discussed in detail in a previous work [40]. Comparable results were obtained for similar glass compositions and direct evidence for the formation of Sr

vacancies can be found in reference [30], where no clear evidence of O vacancies was detected by XRD or ND. The Dy-O bond distance is similar for both Ls-1Eu-0.5Dy and L-1Eu-0.5Dy samples (within the margin of error), whereas the Debye-Waller factor (σ^2) is slightly higher in the former. On considering the results of the Eu L₃-edge, this indicates that the local environment around Eu and Dy ions is similar for the stoichiometric and non-stoichiometric glass-ceramics, with the most notable being the higher fraction of Eu²⁺ stabilised in the non-stoichiometric composition.

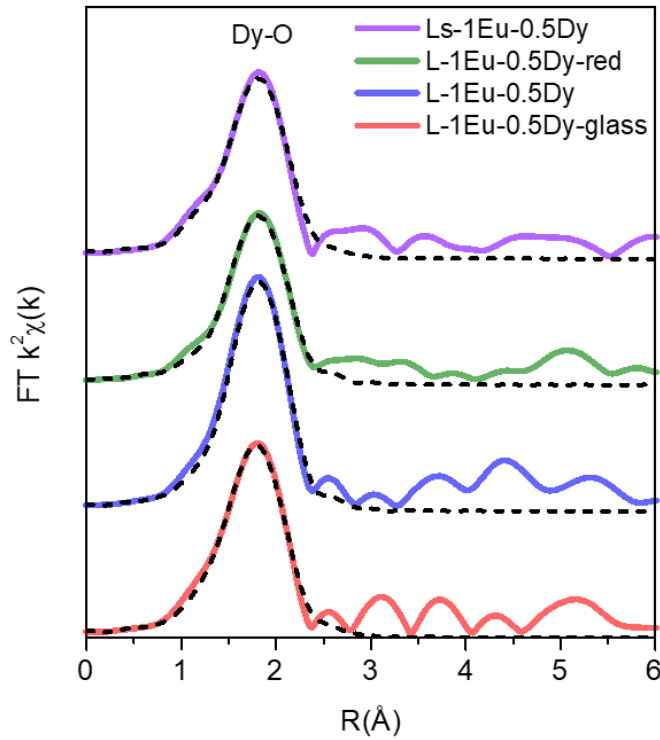


Figure 9. Fourier Transform (FT) of $k^2\chi(k)$ spectra (solid line) at Dy L₂-edge and corresponding first shell fit (dashed line).

3.2. Optical properties

Excitation and emission spectra

Figure 10a exhibits the excitation spectra monitored at 460 nm for the glass-ceramics L-0.5Eu, L-0.5Eu-red, L-1Eu-0.5Dy and L-1Eu-0.5Dy-red. All samples show two excitation peaks at 355 and 400 nm. The Eu-doped samples also show two more pronounced excitation peaks at 315 and 420 nm. Figure 10b shows the fluorescence emission spectra of these samples under excitation at 365 nm. A fluorescence emission band with two maxima at 460 nm and 467 nm is observed for the Eu/Dy co-doped samples, which is associated with the Eu^{2+} ions of the crystalline phase. For the europium-doped samples, a single emission is observed at 467-469 nm. These peaks are assigned to the $\text{T}_{2g} \rightarrow {}^8\text{S}_{7/2}$ transition, splitting between the T_{2g} and E_g levels of the $4f^65d^1$ state of transition of Eu^{2+} ions in the akermanite crystals [22].

Figure 10c shows the monitored excitation spectra at 460 nm for the glass-ceramics Ls-1Eu-0.5Dy, Ls-1Eu-0.5Dy-red, Ls-0.5Eu and Ls-0.5Eu-red obtained from the stoichiometric composition. All samples exhibit emission peaks around 315, 354 and 398 nm. An additional peak appears at $\lambda = 420$ nm for the two Eu/Dy co-doped samples in both atmospheres. Figure 10d shows the fluorescence emission spectra of these four samples under excitation at 365 nm in air and in a reducing atmosphere. The Eu-doped samples exhibit emission maxima at 435 nm, whereas the Eu/Dy co-doped samples, Ls-1Eu-0.5Dy and Ls-1Eu-0.5Dy-red, display maxima at 470 and 473 nm, respectively.

Although the wavelength of 355 nm is the maximum of the excitation peak, the excitation spectrum of Eu^{2+} is broad enough to excite at 365 nm. In addition, the excitation of the 365 nm lamp has a higher intensity than the excitation of the 355 nm lamp, which helps to improve the emission spectra.

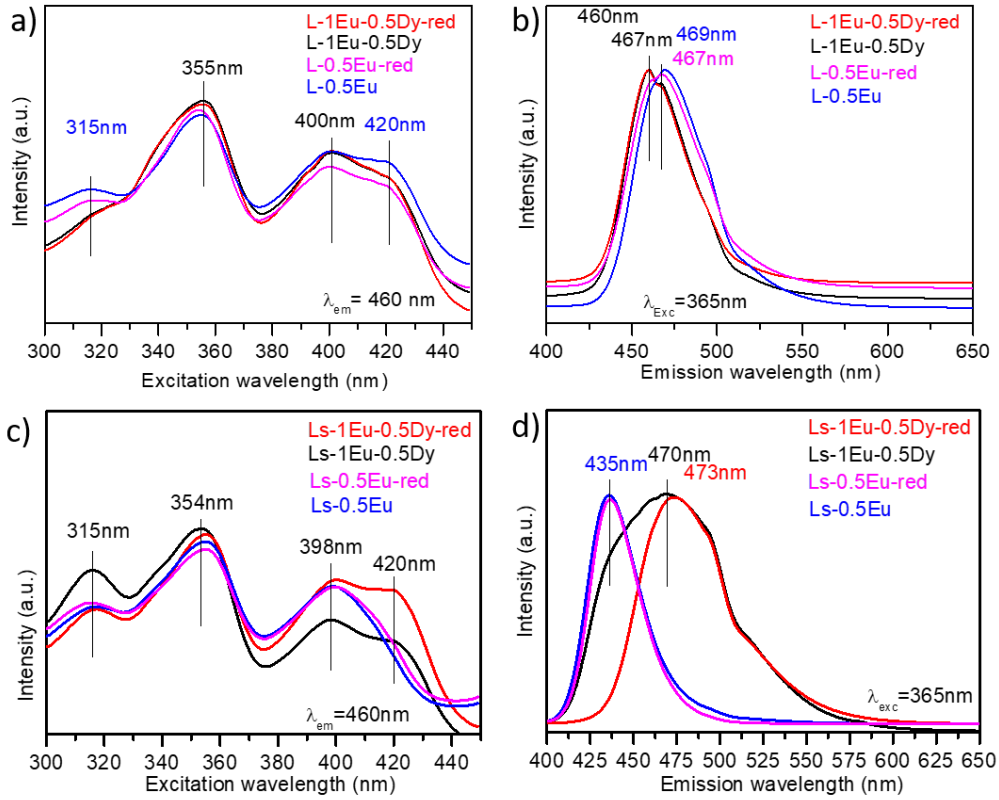


Figure 10. a) Excitation and b) emission spectra of L-0.5Eu, L-0.5Eu-red, L-1Eu-0.5Dy and L-1Eu-0.5Dy-red glass-ceramic samples from non-stoichiometric compositions treated in air and in a reducing atmosphere; c) excitation and d) emission spectra of the Ls-1Eu-0.5Dy, Ls-1Eu-0.5Dy-red, Ls-0.5Eu and Ls-0.5Eu-red samples.

It should be noted that a very weak emission at $\lambda = 617$ nm, attributed to the $^5D_0 \rightarrow ^7F_2$ transition in Eu^{3+} , was discovered in the L-1Eu-0.5Dy glass-ceramic samples (under excitation at $\lambda = 365$ nm or $\lambda = 394$) using detection conditions of much higher sensitivity (X400). This was checked by performing additional studies of L-1Eu-0.5Dy and L-1Eu-0.5Dy glass to evaluate this red emission already detected in G-1Eu-0.5Dy glass-ceramics generated by melting in a gas furnace [29]. However, while XANES detected a considerable amount of Eu^{3+} in all L-1Eu-0.5Dy samples, only a very weak emission from Eu^{3+} in the L-1Eu-0.5Dy glass-ceramic samples can be observed. Excitation spectra taken at a wavelength of $\lambda = 617$ nm for the original L-1Eu-0.5Dy glass revealed Eu^{3+} representative peaks at 394, 460, 525, and 575 nm; however, corresponding peaks were not observed for L-1Eu-0.5Dy glass-ceramic even at increased magnification. As a result, we can corroborate that, while both glass and

glass-ceramic samples have identical percentages of Eu^{2+} and Eu^{3+} in XANES (table 5), the environment in which the europium is present is crucial for red or blue emission to occur. A slightly red emission is obtained in a glassy environment, whereas a blue emission is obtained in the crystalline component of the highly crystallised glass-ceramic.

Persistence behaviour and lifetime

Figure 11 exhibits the glow spectra of L-1Eu-0.5Dy and Ls-1Eu-0.5Dy as a function of temperature with bands at 465 and 475 nm after excitation at 365 nm, respectively, which decrease in intensity as the temperature increases to 50 °C. A very low intensity band around 580-600 nm is also observed (inset of figure 11a), which is practically independent of temperature.

As we reported previously [29], the same composition (1Eu-0.5Dy) prepared by conventional melting in electric and gas furnaces exhibited a low blue emission which passed to red with increasing temperature (the effect is reversible by lowering the temperature again). The blue emission being quenched and only the emission of Eu^{3+} in the remaining glass phase being detected. However, for the L-1Eu-0.5Dy glass-ceramic, we observed blue luminescence, even at 150 °C. This may be due to the higher degree of crystallisation in this material (figure 4) compared to the glasses melted in a conventional gas furnace and corresponding glass-ceramics obtained by sintering and crystallisation of glass powders.

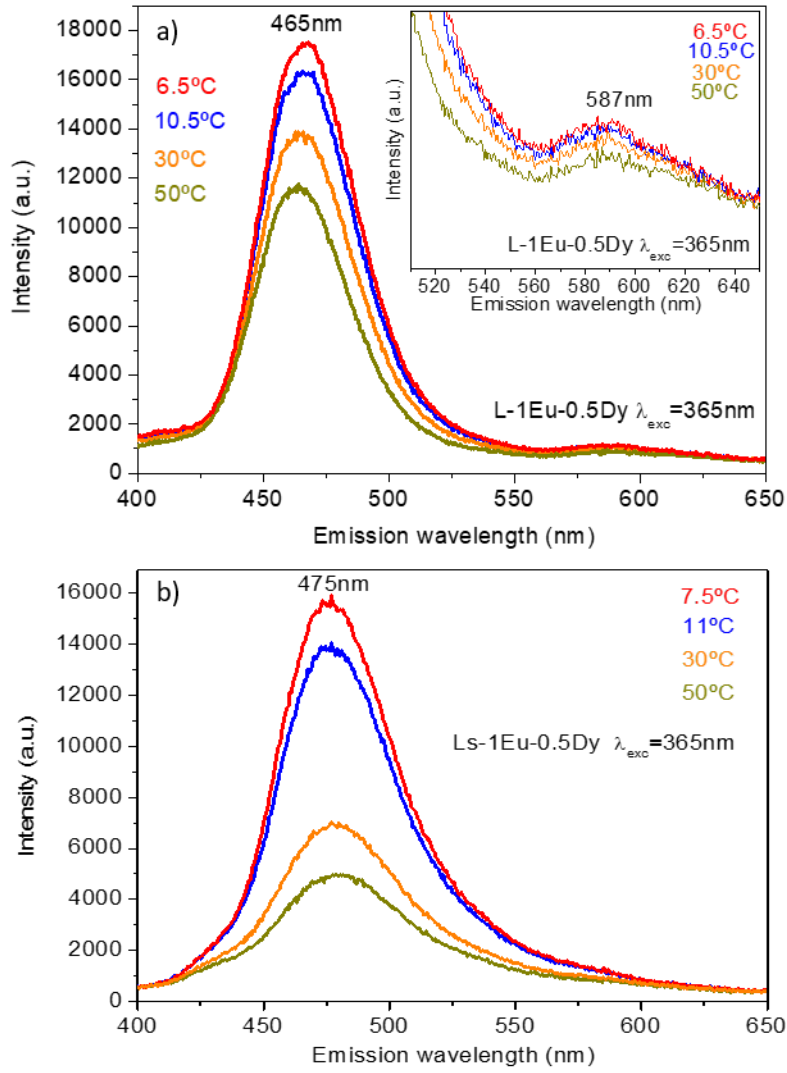


Figure 11. Afterglow spectra of a) L-1Eu-0.5Dy and b) Ls-1Eu-0.5Dy glass-ceramics at different temperatures.

To study the thermal quenching characteristics of phosphors, from figure 11 illustrating the emission spectra of the glass-ceramic L-1Eu-0.5Dy, Ls-1Eu-0.5Dy and the glass-ceramic obtained in previous work from conventional melting measured under various temperatures, the activation energy has been determined. As an important factor for thermal quenching, the activation energy is calculated by the Arrhenius equation [42]:

$$I(T) = \frac{I_0}{1 + A * \exp\left(-\frac{\Delta E}{KT}\right)}$$

where I_0 is the initial emission intensity, $I(T)$ is the intensity at different temperatures, ΔE is the thermal quenching activation energy, A is a constant for a given host, and k is the Boltzmann constant (8.629×10^{-5} eV). Figure 12 represents the plot of $\ln[(I_0/I)] - 1$ versus $1/KT$ and by a linear fit, the value of ΔE was determined. It could be concluded that in the glass-ceramic obtained by conventional melting there is a higher dependence of the intensity variation with temperature (higher activation energy), while in the glass-ceramic L is practically not temperature dependent, which implies a lower tendency to thermal quenching.

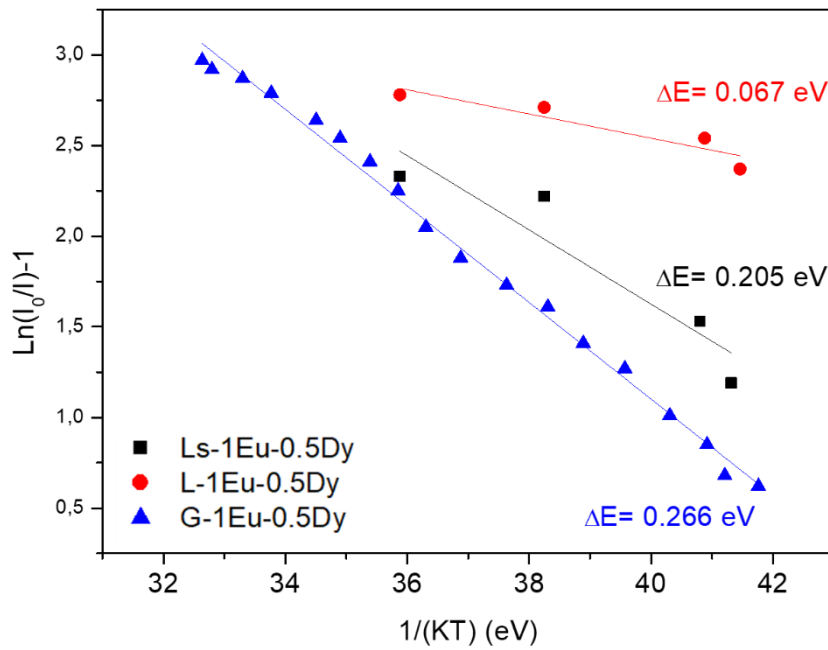


Figure 12. Plot of $\ln(I_0/I) - 1$ versus $1/kT$ of the glass-ceramics L-1Eu-0.5Dy, Ls-1Eu-0.5Dy and G-1Eu-0.5Dy to determine the activation energy.

The decay curves of samples L-1Eu-0.5Dy and Ls-1Eu-0.5Dy have been analysed at different temperatures, an example of which is shown in figure 13 for L-1Eu-0.5Dy at 8.7 °C and 22 °C and Ls-1Eu-0.5Dy 8.5 °C and 22 °C. The curves follow an exponential decay law, with the initial intensity of the sample 150% higher at lower temperatures. Generally, the luminescence decay is constructed from the sum of one or more exponential components, where the first, second and third exponential components corresponds to very fast, slower and much slower emission decays. However, if there are a larger number of traps, the decay arises from the sum of multiple exponentials

[43]. Several studies [8, 44, 45, 46] indicate that the decay may be adjusted to one or two exponentials according to:

$$I(t) = I_0 + A_1^{-t/\tau_1} + A_2^{-t/\tau_2}$$

where $I(t)$ is the intensity for a given time, I_0 represents the final intensity, A_1 and A_2 are constants, t is the decay time, and τ_1 , and τ_2 are the fitting parameters associated with the decay rate [43]. For all studied samples, we determined the best fit to one or two exponentials considering the R^2 values being closest to 1.

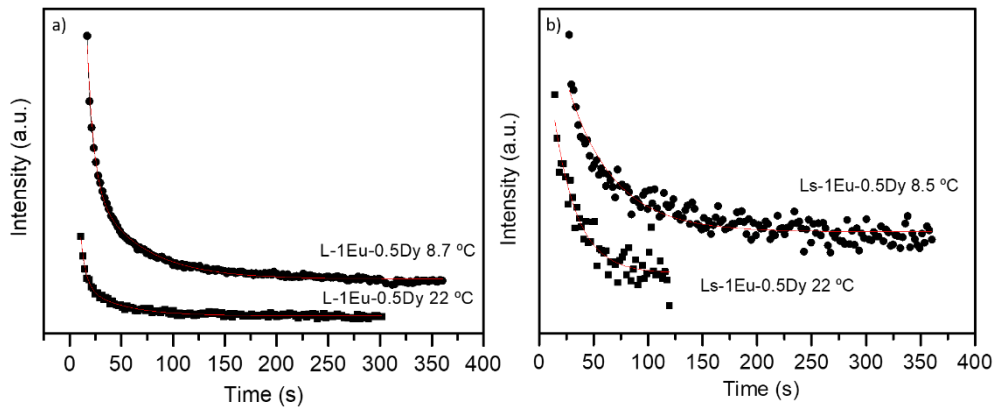


Figure 13. Lifetime of emission collected at 365 nm for the a) L-1Eu-0.5Dy and b) Ls-1Eu-0.5Dy glass-ceramic as a function of temperature.

The decay curves of samples L-1Eu-0.5Dy, L-1Eu-0.5Dy-red, L-0.5Eu and L-0.5Eu-red at 22 °C involving one or two exponentials were analysed. The slowest decay occurs in the sample L-1Eu-0.5Dy over 28.6 s for τ_2 , so the analysis was performed by varying the temperature. The decay times of L-1Eu-0.5Dy at different temperatures are shown in table 6. The decay time of L-1Eu-0.5Dy at 8.7 °C is slightly longer than that of samples measured at RT, and much longer than that of samples measured at higher temperatures. The best decay settings are achieved with an exponential as the temperature increases; in this case, the fastest decay occurs at 50 °C.

Table 6. Fit parameters obtained for the decay curves of Ls-1Eu-0.5Dy at different temperatures.

T (°C)	τ_1 (s)	τ_2 (s)
8.7	6 (1)	49 (2)
11	31 (2)	-
22	29 (2)	-
50	11 (2)	-

As mentioned, the samples Ls-0.5Eu and Ls-0.5Eu-red showed no blue emission under UV light. Furthermore, the emission spectra of these samples (figure 10d) differed, with the maximum at 435 nm, so no decay analysis has been performed. The decay times at 22 °C for the stoichiometric samples Ls-1Eu-0.5Dy and Ls-1Eu-0.5Dy-red have been analysed, where the best fit for the samples at RT was obtained with an exponential, with I_0 and decay similar for the two samples around 20 s.

The decay times for Ls-1Eu-0.5Dy at various temperatures are listed in table 7. One exponentials were used to fit the samples because the decay is very fast in all cases. At lower temperatures, the sample decays much slower than at higher temperatures. In the Ls samples, the fastest decay also occurs at 50 °C.

Table 7. Fit parameters obtained for the exponential decay curves of the sample Ls-1Eu-0.5Dy at different temperatures.

T (°C)	τ_1 (s)
8.5	42 (2)
11	28 (3)
22	21 (2)
50	2 (1)

The non-stoichiometric glass-ceramic L-1Eu-0.5Dy appears to be the most promising. This sample showed the highest initial intensity in comparison to the other compositions, and its intensity increases by around 150 percent at 8.7 °C compared to room temperature. Moreover, this sample showed the longest persistent blue emission, both at room temperature (41 s) and at low temperatures (82 s), as well as the slowest decay curves ($\tau_2=49$ s).

The persistence of stoichiometric glass ceramics was inferior, possibly due to traces of the $\text{Sr}_3\text{MgSi}_2\text{O}_8$ phase found by XRD.

In this investigation, the most persistent glass-ceramic was L-1Eu-0.5Dy with a persistence time of 41 s and 82 s at RT at 0 °C, respectively, and with a value of $\tau_1=29$ s at RT and $\tau_1=6$ and $\tau_2=49$ at 8.7 °C. In comparison with the $\text{Ba}_2\text{Si}_3\text{O}_8: \text{Eu}^{2+}, \text{Dy}^{3+}$ glass-ceramic obtained by K. Asami et al. [4] using a reducing atmosphere, we observe that our persistence times are much shorter. In their case with a heat treatment at 1100 °C for 6 h in 95% N_2 /5% H_2 , a persistence time of 616 min was reached. On the other hand, in the case of the same $\text{Sr}_2\text{MgSi}_2\text{O}_7: \text{Eu}^{2+}, \text{Dy}^{3+}$ phase investigated by H. Wu et al. [8], obtained by solid-state reaction, also in a reducing atmosphere, the crystallised material reached values of $\tau_1=42$ s and $\tau_2=167$ s.

Hence, in both cases, higher values are reached and a reducing atmosphere is employed. However, in our materials, the lifetime and/or persistence values are not higher in a reducing atmosphere.

Conclusions

Glass beads of the $\text{Sr}_2\text{MgSi}_2\text{O}_7$ stoichiometric composition and a non-stoichiometric composition with higher SiO_2/SrO ratio doped with $\text{Eu}_2\text{O}_3/\text{Dy}_2\text{O}_3$ were prepared through aerodynamic levitation. Akermanite is the main crystalline phase on crystallisation and the glass-ceramics obtained from the non-stoichiometric starting composition exhibited larger microcrystals.

The relative Eu^{2+} and Eu^{3+} contents do not change significantly after crystallisation of the samples. Initially, Eu^{2+} is already present in the base glass, but in the corresponding glasses and glass ceramics there is mostly Eu^{3+} . A crystalline environment in the akermanite microcrystals promotes blue emission from the RE ions.

Non-stoichiometric Eu/Dy co-doped glass beads after crystallisation on thermal treatment in air provided the longest blue-emission afterglow (approximately 40 and 82 s at RT and 0 °C, respectively) observed by the naked eye. This persistence time is shorter than the same glass-ceramic compositions prepared by conventional melting in a gas furnace. Nevertheless, it is notable that the emission of the samples obtained by levitation remained blue after increasing the temperature while, in the analogous samples prepared by conventional melting, the samples emitted red from temperatures above 50 °C.

In the Eu/Dy-doped non-stoichiometric composition, the decay curves fit better to a biexponential relationship with decreasing temperature. After irradiation at $\lambda_{\text{exc}} = 365$ nm, the Eu^{2+} band in the emission spectrum intensifies with decreasing temperature. The decay curves and parameters obtained for the non-stoichiometric samples reveal a slower decay in the case of Eu/Dy co-doped samples treated in air and the initial intensity is higher, in agreement with the times observed with the naked eye.

The final microstructure of the non-stoichiometric glass-ceramics and the greater incorporation of Eu/Dy in larger akermanite crystals compared to those of the stoichiometric composition both increase the luminescence intensity and persistence by 67 and 80%, respectively.

Acknowledgements

Funding from MICINN under project PID2020-115419GB-C-21/C-22/AEI/10.13039/501100011033 is acknowledged. This work has received support from the French Agency for Research (Agence Nationale de la Recherche, ANR) through the Equipex Planex ANR-11-EQPX-36. XAS experiments were performed at the BL22-CLAESS beamline at the ALBA synchrotron with the collaboration of ALBA staff under the experiment number AV – 2020094476.

Bibliography

- [1] T. Matsuzawa, A New Long Phosphorescent Phosphor with High Brightness, $\text{SrAl}_2\text{O}_4:\text{Eu}^{2+}, \text{Dy}^{3+}$, J. Electrochem. Soc. 143 (1996) 2670. <https://doi.org/10.1149/1.1837067>.
- [2] J.R. Encinar, A. Sanz-Medel, J.M. Costa-Fernández., M.T. Fernández-Argüelles, Phosphorescence. Principles and Instrumentation, Vol. 8, 2005.
- [3] L. Fernández-Rodríguez, A. Durán, M.J. Pascual, Silicate-based persistent phosphors, Open Ceram. 7 (2021) 100150. <https://doi.org/10.1016/j.oceram.2021.100150>.
- [4] K. Asami, J. Ueda, S. Tanabe, Long persistent luminescence and blue photochromism in Eu^{2+} - Dy^{3+} co-doped barium silicate glass ceramic phosphor, J. Lumin. 207 (2019) 246–250. <https://doi.org/10.1016/j.jlumin.2018.11.006>.
- [5] J. Duan, Y. Liu, X. Pan, Y. Gu, X. Zheng, W. Li, W. Wang, C. Wang, J. Yu, Transparency, photoluminescence and X-ray luminescence study of Eu^{3+} doped

- mayenite glass, *Mater. Lett.* 173 (2016) 102–106.
<https://doi.org/10.1016/j.matlet.2016.03.039>.
- [6] S. Liu, Y. Liang, M. Tong, D. Yu, Y. Zhu, X. Wu, C. Yan, Photoluminescence properties of novel white phosphor of Dy³⁺-doped LaBSiO₅ glass, *Mater. Sci. Semicond. Process.* 38 (2015) 266–270.
<https://doi.org/10.1016/j.mssp.2015.04.009>.
- [7] J. Xu, S. Tanabe, Persistent luminescence instead of phosphorescence: History, mechanism, and perspective, *J. Lumin.* 205 (2019) 581–620.
<https://doi.org/10.1016/j.jlumin.2018.09.047>.
- [8] H. Wu, Y. Hu, Y. Wang, B. Zeng, Z. Mou, L. Deng, W. Xie, Influence on luminescent properties of the Sr₂MgSi₂O₇: Eu²⁺ by Dy³⁺, Nd³⁺ co-doping, *J. Alloys Compd.* 486 (2009) 549–553.
<https://doi.org/10.1016/j.jallcom.2009.07.002>.
- [9] I. Chen, T. Chen, Sol-gel synthesis and the effect of boron addition on the phosphorescent properties of SrAl₂O₄:Eu²⁺, Dy³⁺ phosphors, *J. Mater. Res.* (2001) 16(3) 644–651. <https://doi.org/DOI: 10.1557/JMR.2001.0122>.
- [10] X. Wei, Y. Shen, G. Zuo, L. Hou, Y.Z. Meng, F. Li, Preparation of porous Sr₂MgSi₂O₇:Eu²⁺, Dy³⁺ energy storage carriers via sol-hydrothermal synthesis, *Ceram. Int.* 41 (2015) 13872–13877.
<https://doi.org/10.1016/j.ceramint.2015.06.144>.
- [11] Y. Xu, D. Chen, Combustion synthesis and photoluminescence of Sr₂MgSi₂O₇:Eu, Dy long lasting phosphor nanoparticles, *Ceram. Int.* 34 (2008) 2117–2120. <https://doi.org/10.1016/j.ceramint.2007.08.012>.
- [12] L. Pan, S. Liu, X. Zhang, O. Oderinde, F. Yao, G. Fu, Optimization method for blue Sr₂MgSi₂O₇:Eu²⁺, Dy³⁺ phosphors produced by microwave synthesis route, *J. Alloys Compd.* 737 (2018) 39–45.
<https://doi.org/10.1016/j.jallcom.2017.11.343>.
- [13] H. Duan, Y.Z. Dong, Y. Huang, Y.H. Hu, X.S. Chen, The important role of oxygen vacancies in Sr₂MgSi₂O₇ phosphor, *Phys. Lett. Sect. A Gen. At. Solid State Phys.* 380 (2016) 1056–1062.
<https://doi.org/10.1016/j.physleta.2016.01.001>.
- [14] I.P. Sahu, D.P. Bisen, N. Brahme, R.K. Tamrakar, Enhanced luminescence performance of Sr₂MgSi₂O₇:Eu²⁺ blue long persistence phosphor by co-doping with Ce³⁺ ions, *J. Mater. Sci. Mater. Electron.* 27 (2016) 554–569.

<https://doi.org/10.1007/s10854-015-3789-2>.

- [15] T. Aitasalo, J. Hassinen, J. Hölsä, T. Laamanen, M. Lastusaari, M. Malkamäki, J. Niittykoski, P. Novák, Synchrotron radiation investigations of the $\text{Sr}_2\text{MgSi}_2\text{O}_7\text{:Eu}^{2+}, \text{R}^{3+}$ persistent luminescence materials, *J. Rare Earths*. 27 (2009) 529–538. [https://doi.org/10.1016/S1002-0721\(08\)60283-5](https://doi.org/10.1016/S1002-0721(08)60283-5).
- [16] T. Aitasalo, P. Dereń, J. Hölsä, H. Jungner, J.C. Krupa, M. Lastusaari, J. Legendziewicz, J. Niittykoski, W. Stręk, Persistent luminescence phenomena in materials doped with rare earth ions, *J. Solid State Chem.* 171 (2003) 114–122. [https://doi.org/10.1016/S0022-4596\(02\)00194-9](https://doi.org/10.1016/S0022-4596(02)00194-9).
- [17] T. Nakanishi, Y. Katayama, J. Ueda, T. Honma, S. Tanabe, T. Komatsu, Fabrication of $\text{Eu:SrAl}_2\text{O}_4$ -based glass ceramics using frozen sorbet method, *J. Ceram. Soc. Japan*. 119 (2011) 609–615. <https://doi.org/10.2109/jcersj2.119.609>.
- [18] T. Nakanishi, K. Watanabe, J. Ueda, K. Fushimi, S. Tanabe, Y. Hasegawa, Enhanced light storage of SrAl_2O_4 glass-ceramics controlled by selective europium reduction, *J. Am. Ceram. Soc.* 98 (2014) 423–429. <https://doi.org/10.1111/jace.13312>.
- [19] Q. Fei, C. Chang, D. Mao, Luminescent properties of $\text{Sr}_2\text{MgSi}_2\text{O}_7$ and $\text{Ca}_2\text{MgSi}_2\text{O}_7$ long lasting phosphors activated by Eu^{2+} , Dy^{3+} , 390 (2005) 133–137. <https://doi.org/10.1016/j.jallcom.2004.06.096>.
- [20] H.F. Brito, J. Hölsä, H. Jungner, T. Laamanen, M. Lastusaari, M. Malkamäki, L.C.V. Rodrigues, Persistent luminescence fading in $\text{Sr}_2\text{MgSi}_2\text{O}_7\text{:Eu}^{2+}, \text{R}^{3+}$ materials: a thermoluminescence study, *Opt. Mater. Express*. 2 (2012) 287. <https://doi.org/10.1364/OME.2.000287>.
- [21] S. Nishiura, S. Tanabe, Preparation and luminescence properties of glass ceramics precipitated with $\text{M}_2\text{MgSi}_2\text{O}_7\text{:Eu}^{2+}$ ($\text{M} = \text{Sr}, \text{Ca}$) phosphor for white light source, *IEEE J. Sel. Top. Quantum Electron.* 15 (2009) 1177–1180. <https://doi.org/10.1109/JSTQE.2009.2014175>.
- [22] L. Wondraczek, S. Krolkowski, P. Nass, Europium partitioning, luminescence re-absorption and quantum efficiency in (Sr,Ca) akermanite–feldspar bi-phasic glass ceramics, *J. Mater. Chem. C*. (2013) 4078–4086. <https://doi.org/10.1039/c3tc30609g>.
- [23] K. Yoshimoto, A. Masuno, H. Inoue, Y. Watanabe, Transparent and high refractive index $\text{La}_2\text{O}_3\text{-WO}_3$ glass prepared using containerless processing, *J. Am. Ceram. Soc.* 95 (2012) 3501–3504. <https://doi.org/10.1111/j.1551->

2916.2012.05439.x.

- [24] A.J. Fernandez-Carrion, K. Al Saghir, E. Veron, A.I. Becerro, F. Porcher, W. Wisniewski, G. Matzen, F. Fayon, M. Allix, Local Disorder and Tunable Luminescence in $\text{Sr}_{1-x/2}\text{Al}_{2-x}\text{Si}_x\text{O}_4$ ($0.2 \leq x \leq 0.5$) Transparent Ceramics, *Inorg. Chem.* 56 (2017) 14446–14458. <https://doi.org/10.1021/acs.inorgchem.7b01881>.
- [25] M. Zhang, H. Wen, J. Yu, F. Ai, H. Yu, X. Pan, H. Shao, M. Tang, L. Gai, Investigation of upconversion luminescence in $\text{Er}^{3+}/\text{Yb}^{3+}$ co-doped Nb_2O_5 -based glasses prepared by aerodynamic levitation method, *Opt. Mater. Express.* 7 (2017) 3222. <https://doi.org/10.1364/ome.7.003222>.
- [26] M. Zhang, H. Wen, X. Pan, J. Yu, H. Shao, M. Tang, L. Gai, F. Ai, Study on novel high refractive index La_2O_3 - Lu_2O_3 - TiO_2 glasses prepared by aerodynamic levitation method, *Mater. Lett.* 222 (2018) 5–7. <https://doi.org/10.1016/j.matlet.2018.03.120>.
- [27] K. Shinozaki, T. Honma, M. Affatigato, T. Komatsu, Long afterglow in hexagonal $\text{SrAl}_2\text{O}_4:\text{Eu}^{2+}$, Dy^{3+} synthesized by crystallization of glass and solidification of supercooled melts, *J. Lumin.* 177 (2016) 286–289. <https://doi.org/10.1016/j.jlumin.2016.05.013>.
- [28] V. Castaing, C. Monteiro, A.D. Sontakke, K. Asami, J. Xu, A.J. Fernández-Carrión, M.G. Brik, S. Tanabe, M. Allix, B. Viana, Hexagonal $\text{Sr}_{1-x/2}\text{Al}_{2x}\text{Si}_x\text{O}_4:\text{Eu}^{2+}$, Dy^{3+} transparent ceramics with tuneable persistent luminescence properties, *Dalt. Trans.* 49 (2020) 16849–16859. <https://doi.org/10.1039/d0dt03137b>.
- [29] L. Fernández-Rodríguez, D. Levy, M. Zayat, J. Jiménez, G.C. Mather, A. Durán, M.J. Pascual, Processing and luminescence of Eu/Dy-doped $\text{Sr}_2\text{MgSi}_2\text{O}_7$ glass-ceramics, *J. Eur. Ceram. Soc.* 41 (2021) 811–822. <https://doi.org/10.1016/j.jeurceramsoc.2020.08.038>.
- [30] L. Simonelli, C. Marini, W. Olszewski, M. Avila Perez, N. Ramanan, G. Guilera, V. Cuartero, K. Klementiev, CLAEISS: The hard X-ray absorption beamline of the ALBA CELLS synchrotron, *Cogent Phys.* 3 (2016). <https://doi.org/10.1080/23311940.2016.1231987>.
- [31] B. Ravel, M. Newville, ATHENA, ARTEMIS, HEPHAESTUS: Data analysis for X-ray absorption spectroscopy using IFEFFIT, *J. Synchrotron Radiat.* 12 (2005) 537–541. <https://doi.org/10.1107/S0909049505012719>.
- [32] D. Haskel, FLUO: Correcting XANES for self-absorption effects, (n.d.). <https://www3.aps.anl.gov/haskel/fluo.html>.

- [33] R. Takamori, T.; Roy, Metastable Modification of SrSiO_3 , 203 (1972) 1972.
- [34] S. Rodríguez López, Propiedades termo-mecánicas de sellos vitrocerámicos del sistema $\text{RO-MgO-B}_2\text{O}_3\text{-SiO}_2$ ($\text{R}=\text{Ba, Sr}$) para SOFC, PhD thesis UAM, 2016.
- [35] M. Kimata, The structural properties of synthetic Sr-akermanite, $\text{Sr}_2\text{MgSi}_2\text{O}_7$, Zeitschrift Für Krist. Mater. 304 (1983) 295–304. <https://doi.org/10.1524/zkri.1983.163.14.295>.
- [36] Y. Yonesaki, T. Takei, N. Kumada, N. Kinomura, Crystal structure of Eu^{2+} -doped $\text{M}_3\text{MgSi}_2\text{O}_8$ (M: Ba, Sr, Ca) compounds and their emission properties, J. Solid State Chem. 182 (2009) 547–554. <https://doi.org/10.1016/j.jssc.2008.11.032>.
- [37] J. Hanuza, M. Ptak, M. Mączka, K. Hermanowicz, J. Lorenc, A.A. Kaminskii, Polarized IR and Raman spectra of $\text{Ca}_2\text{MgSi}_2\text{O}_7$, $\text{Ca}_2\text{ZnSi}_2\text{O}_7$ and $\text{Sr}_2\text{MgSi}_2\text{O}_7$ single crystals: Temperature-dependent studies of commensurate to incommensurate and incommensurate to normal phase transitions, J. Solid State Chem. 191 (2012) 90–101. <https://doi.org/10.1016/j.jssc.2012.02.051>.
- [38] Y. Yonezaki, $(\text{Ba, Sr})_3\text{MgSi}_2\text{O}_8$ structure change caused by Ba/Sr replacement, Powder Diffr. 30 (2015) 40–51. <https://doi.org/10.1017/S0885715614000803>.
- [39] H. Kojitani, M. Kido, M. Akaogi, Rietveld analysis of a new high-pressure strontium silicate SrSi_2O_5 , (2005) 32: 290-294. <https://doi.org/10.1007/s00269-005-0467-6>.
- [40] L. Fernández-Rodríguez, G. Gorni, G.C. Mather, S. Savvin, G.J. Cuello, A. Durán, M.J. Pascual, X-ray absorption spectroscopy and neutron-diffraction study of persistent luminescent $\text{Sr}_2\text{MgSi}_2\text{O}_7$ glass-ceramics, Acta Mater. 215 (2021) 117080. <https://doi.org/10.1016/j.actamat.2021.117080>.
- [41] J.J. Joos, K. Korthout, L. Amidani, P. Glatzel, D. Poelman, P.F. Smet, Identification of $\text{Dy}^{3+}/\text{Dy}^{2+}$ as Electron Trap in Persistent Phosphors, Phys. Rev. Lett. 125 (2020) 33001. <https://doi.org/10.1103/PhysRevLett.125.033001>.
- [42] J. Zhang, G. Chen, A long-persistent phosphor $\text{Sr}_3\text{MgSi}_2\text{O}_{8-1.5x}\text{N}_x$: Eu^{2+} , Dy^{3+} , Mn^{2+} based on white LEDs applications, J. Lumin. 211 (2019) 69–75. <https://doi.org/10.1016/j.jlumin.2019.03.027>.
- [43] T. Jiang, H. Wang, M. Xing, Y. Fu, Y. Peng, X. Luo, Luminescence decay evaluation of long-afterglow phosphors, Phys. B Condens. Matter. 450 (2014) 94–98. <https://doi.org/10.1016/j.physb.2014.04.080>.
- [44] C.Y. Tsai, J.W. Lin, Y.P. Huang, Y.C. Huang, Modeling and Assessment of

- Long Afterglow Decay Curves, Sci. World J. 2014 (2014).
<https://doi.org/10.1155/2014/102524>.
- [45] Y. Lin, Z. Tang, Z. Zhang, C.W. Nan, Luminescence of Eu^{2+} and Dy^{3+} activated $\text{R}_3\text{MgSi}_2\text{O}_8$ -based (R=Ca, Sr, Ba) phosphors, J. Alloys Compd. 348 (2003) 76–79. [https://doi.org/10.1016/S0925-8388\(02\)00796-X](https://doi.org/10.1016/S0925-8388(02)00796-X).
- [46] H. Wu, Y. Hu, X. Wang, Investigation of the trap state of $\text{Sr}_2\text{MgSi}_2\text{O}_7$: Eu^{2+} , Dy^{3+} phosphor and decay process, Radiat. Meas. 46 (2011) 591–594. <https://doi.org/10.1016/j.radmeas.2011.04.023>.

Appendix

Figure A.1 shows the ATD of the Ls-1Eu-0.5Dy sample. The T_g appears around 750 ± 2 °C; there are two main crystallisation peaks at 897 and 908 °C.

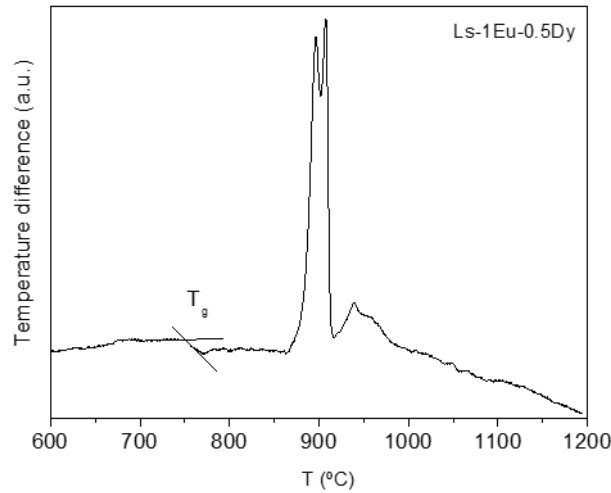


Figure A.1 DTA corresponding to Ls-1Eu-0.5Dy glass powder ($< 40\mu\text{m}$).

Figure A.2 shows in-situ XRD diffractograms of L-undoped glass. The $\text{Sr}_2\text{MgSi}_2\text{O}_7$ phase (ICDD: 75-1736) crystallises at 850 °C. Other secondary phases such as SrSiO_3 , SrO_2 and an unidentified phase are also present at 1100 °C.

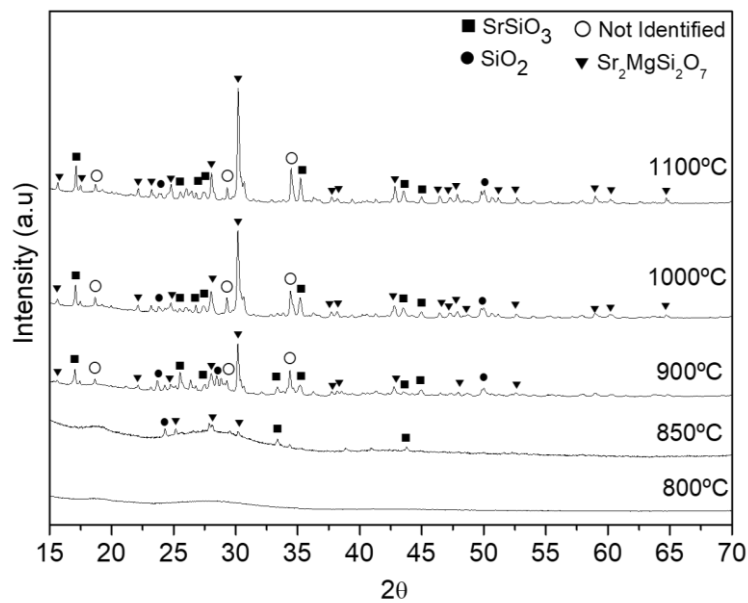


Figure A.2 In-situ high-temperature XRD patterns of the L-undoped glass.

Figure A.3. Experimental (red circles), calculated (continuous black line) and difference (continuous blue line) X-ray powder diffraction profiles of Ls-1E-0.5Dy. The Bragg peaks of $\text{Sr}_2\text{MgSi}_2\text{O}_7$ and $\text{Sr}_3\text{MgSi}_2\text{O}_8$ are indicated by top and bottom vertical bars (in green), respectively.

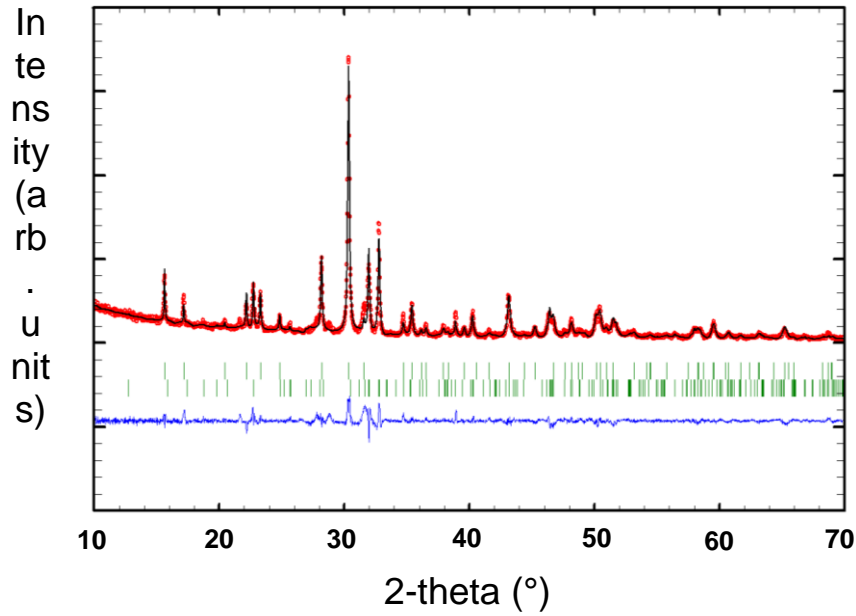


Figure A.3. XRD pattern and corresponding Rietveld refinement for Ls-1Eu-0.5Dy glass-ceramics.

Raman spectra at RT of L-1Eu-0.5Dy, Ls-1Eu-0.5Dy and Ls-0.5Eu glass-ceramics are shown in figure A.4. The peaks that appear correspond to the $\text{Sr}_2\text{MgSi}_2\text{O}_7$ phase [37] for most of the samples, as observed for L-1Eu-0.5Dy and Ls-1Eu-0.5Dy. However, for the sample Ls-0.5Eu and Ls-0.5Eu-red, other peaks appear between $350\text{--}400\text{ cm}^{-1}$ and 550 cm^{-1} which have not been identified.

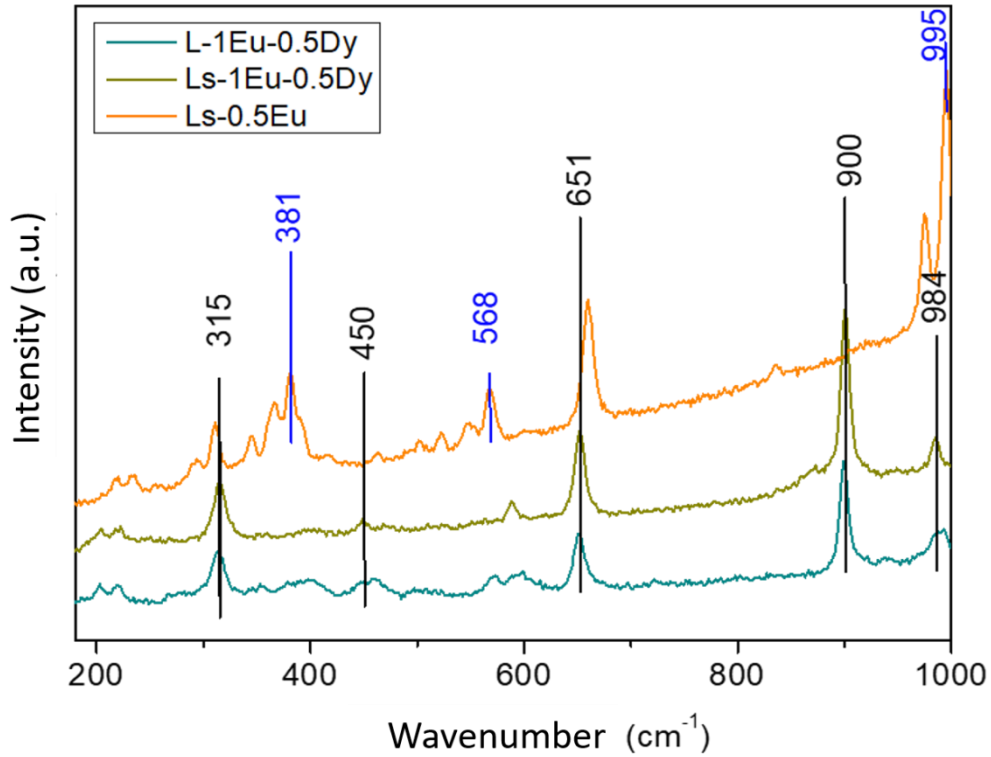


Figure A.4. Raman spectrum of L-1Eu-0.5Dy, Ls-1Eu-0.5Dy and Ls-0.5Eu glass-ceramics.

Figure A.5 is a cut and polished section of the glass-ceramic L-1-Eu-0.5 Dy. Figure A.5a shows how the crystallization is superficial and decreases from the outside towards the inside, while figure A.5b shows the central part of the section. In the central part much smaller crystals are observed than in the superficial unpolished part of the bead that have been seen in figure 4.

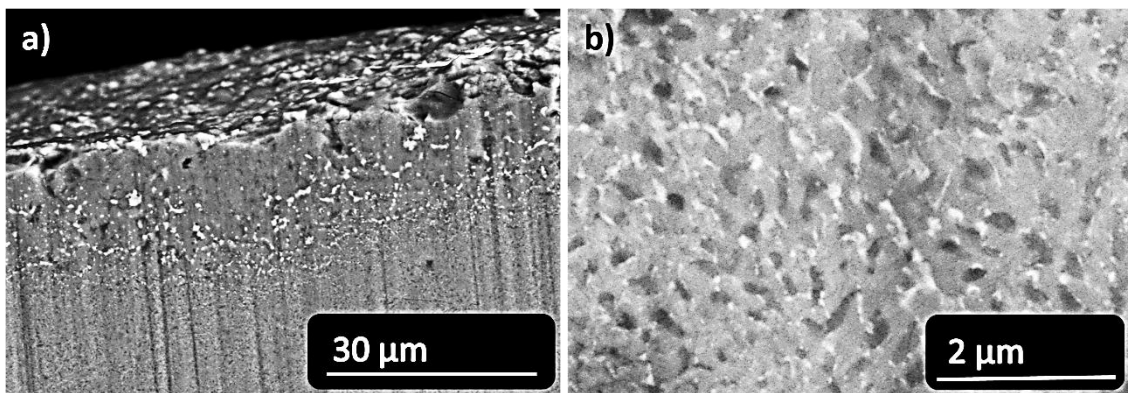


Figure A.5. SEM analysis of the L-1Eu-0.5Dy bead. a) cut bead where the surface growth of the crystals can be observed and b) central part of the cut and polished bead.

Figure A.6. Peak fitting (red line) of the normalized absorption for the L-1Eu-0.5Dy sample (blue circles). The lineshape used for the fitting is a pseudo Voigt function (PVF) and an arctangent was used to model the transition to the continuum.

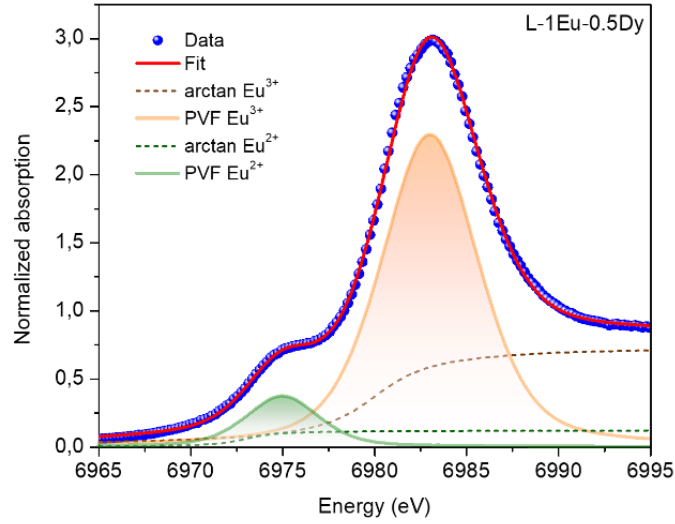


Figure A.6. Peak fitting of Eu L₃-edge XANES spectrum using Pseudo-Voigt (PVF) and arctan functions.

Table A.1. Results of the first-shell fit of FT $k^2\chi(k)$ spectra at the Eu L₃-edge; N is the coordination number, R is the bond distance and σ^2 is the Debye-Waller factor.

Sample	Bond	N	R(Å)	σ^2 (10^{-3} Å)
L-1Eu-0.5Dy-glass	Eu-O	6	2.326±0.012	13.7±1.6
L-1Eu-0.5Dy	Eu-O	6	2.333±0.015	13.8±1.1
L-1Eu-0.5Dy -red	Eu-O	6	2.338±0.015	19.7±1.8
Ls-1Eu-0.5Dy	Eu-O	6	2.342±0.014	12.8±1.6

Table A.2. Results of the first-shell fit of FT $k^2\chi(k)$ spectra at the Dy L₂-edge; N is the coordination number, R is the bond distance and σ^2 is the Debye-Waller factor.

Sample	Bond	N	R(Å)	σ^2 (10^{-3} Å)
L-1Eu-0.5Dy-glass	Dy-O	6	2.270±0.016	9.5±1.4
L-1Eu-0.5Dy	Dy-O	6	2.286±0.015	6.7±1.1
L-1Eu-0.5Dy-red	Dy-O	6	2.283±0.015	10.5±1.6
Ls-1Eu-0.5Dy	Dy-O	6	2.305±0.016	9.5±1.6